Highlights

Large-scale sea surface temperature gradients govern westerly moisture transport in western Ecuador during the Plio-Pleistocene

David Fastovich, Tripti Bhattacharya, Lina C. Pérez-Ángel, Natalie J. Burls, Ran Feng, Scott Knapp, Theodor Mayer

- Hydrogen isotopes in precipitation encode westerly water vapor transport in western Ecuador.
- Westerly water vapor transport weakened during the early Pliocene.
- Westerly water vapor transport responds to regional sea surface temperature gradients.
- Westerly wind weakening at ~3 Ma may be caused by Northern Hemisphere cooling.
- Projected changes to the Choco jet will influence hydroclimate and landslides.

Large-scale sea surface temperature gradients govern westerly moisture transport in western Ecuador during the Plio-Pleistocene

David Fastovich[a,*], Tripti Bhattacharya[a], Lina C. Pérez-Ángel[b], Natalie J. Burls[c], Ran Feng[d], Scott Knapp[c], Theodor Mayer[d]

[a]*Department of Earth and Environmental Sciences, Syracuse University, Syracuse, NY, USA*
[b]*Institute at Brown for Environment and Society and Department of Earth, Environmental and Planetary Sciences, Brown University, Providence, RI, USA*
[c]*Department of Atmospheric, Oceanic, and Earth Sciences, George Mason University, Fairfax, VA, USA*
[d]*Department of Earth Sciences, University of Connecticut, University of Connecticut, Storrs, CT, USA*

Abstract

The cross-equatorial southwesterly winds from the eastern equatorial Pacific direct moisture toward the Pacific coast of northwestern South America, where subsequent orographic lifting creates the wettest regions in the world. The Choco low-level jet is emblematic of broader westerly winds in this region and is projected to weaken by the end of the 21st century, but climate models show considerable disagreement about the extent of weakening. Using contemporary observations, we demonstrate that the configuration of westerly winds in the eastern equatorial Pacific is reflected by hydrogen isotopes in precipitation (δD_p) in western Ecuador. As westerly winds strengthen, δD_p increases from greater transport of δD_{vapor} enriched in deuterium from the Eastern Pacific Warm Pool. We apply this framework to a new record of reconstructed δD_p using leaf waxes in ocean sediments off the coast of Ecuador (ODP1239, 0°40.32′ S, 82°4.86′ W) that span the Plio-Pleistocene. Low δD_p in the early Pliocene indicates weak westerly water vapor transport in a warmer climate state, which is attributed to a low sea surface

*Corresponding Author
Email address: dfastovi@syr.edu (David Fastovich)

temperature gradient between the cold tongue and off-equatorial regions in the eastern equatorial Pacific. Near 3 Ma, westerly water vapor transport weakens, possibly as a result of shifts in the Intertropical Convergence Zone forced by high latitude Northern Hemisphere cooling. In complementary isotope-enabled climate simulations, a weak Choco jet and westerly water vapor transport in the early Pliocene are matched by a decrease in δD_p and hydroclimate changes in western Ecuador. Precipitation from the Choco jet can cause deadly landslides and weakened westerly winds in the early Pliocene implies a southward shift of these hazards along the Pacific coast of northwestern South America in the future.

Keywords:
leaf waxes, isotopes of precipitation, Pliocene, hydroclimate, South America

---

1. Introduction

The Western Cordillera of northwestern South America contains some of the wettest regions in the world (Poveda and Mesa, 2000), supporting high biodiversity (Rangel et al., 2018; Myers et al., 2000). Interannual changes in precipitation can yield droughts (Vicente-Serrano et al., 2017) and floods (Waylen and Caviedes, 1986). During flood events, high rainfall and extreme topography create ideal conditions for mass wasting. Fatal landslides are common along the Western Cordillera of the tropical Andes and have caused thousands of fatalities in the last century that disproportionally impact vulnerable populations (Garcia-Delgado et al., 2022).

Increases in regional precipitation amount and seasonality are expected in the coming century (Ramirez-Villegas et al., 2012; Vuille et al., 2008). This could increase the prevalence of landslides, which have accelerated in the last 20 years (Garcia-Delgado et al., 2022). However, accurate projections of precipitation-related risks are hampered by uncertain climate projections (Sierra et al., 2021).

Hydroclimate variability in the region is tightly linked to cross-equatorial westerly water vapor transport from the eastern equatorial Pacific (Hoyos et al., 2018; Poveda et al., 2006; Poveda and Mesa, 2000; Sierra et al., 2021). Within this flow is a concentrated low-level jet called the Choco low-level jet, though westerly flow is not confined to this feature (Hoyos et al., 2018; Poveda et al., 2006; Poveda and Mesa, 2000; Sierra et al., 2021; Xie and Philander, 1994). Westerly winds are lofted by tropical easterlies and orographic lift-

ing by the Western Cordillera of the Andes facilitating deep convection and intense precipitation (Poveda and Mesa, 2000). Current generation climate models struggle to reproduce historic features of the Choco jet and westerly flow in general, casting doubt on their ability to predict future changes in regional circulation (Sierra et al., 2015, 2018). This highlights a need to improve our fundamental understanding of atmospheric circulation and moisture transport in this region.

Various paleoclimatic reconstructions suggest that westerly water vapor transport toward northwestern South America is sensitive to the background climate. During the Last Glacial Maximum, the sea surface temperature (SST)gradient across the Equatorial Front in the eastern equatorial Pacific was greater than present and may have supported a stronger Choco jet (Martínez et al., 2003). Climate simulations of the Little Ice Age demonstrate a similar relationship, linking an intensification of westerly transport to a stronger sea level pressure gradient between the eastern equatorial Pacific and northwestern South America (Sierra et al., 2021). However, insights from past warm climates can shed light on the sensitivity of westerly transport to greenhouse gas forcings. For instance, the Pliocene is a recent geologic epoch with atmospheric carbon dioxide concentrations similar to contemporary levels (Martínez-Botí et al., 2015).

The Pliocene is marked by high SSTs and low SST gradients (meridional and zonal) throughout the Pacific (Tierney et al., 2019). Similar to the Pliocene, contemporary El Niño events also produce a low meridional SST gradient in the eastern tropical Pacific from warming in the cold tongue. In response to this reduced SST gradient, cross-equatorial westerly water vapor transport weakens (Poveda et al., 2006), drying the Pacific coast of Colombia, while increasing precipitation in northern Peru (Hoyos et al., 2019) and the western Ecuadorian lowlands (Morán-Tejeda et al., 2016).

Unfortunately, few paleoclimatic records span the Pliocene in northwestern South America (Etourneau et al., 2010; Grimmer et al., 2018, 2020; Herbert et al., 2016; Lawrence et al., 2006; Seki et al., 2012), only one examines large scale atmospheric circulation (Hovan, 1995), and terrestrial paleoclimate archives in this region are rarer still. Moreover, it is unclear how regional atmospheric circulation is reflected in existing records. This gap in proxy reconstructions precludes identifying changes to westerly moisture transport in the eastern equatorial Pacific in warm climates forced by high greenhouse gas concentrations, which can be constrained through hydroclimate reconstructions during the Pliocene.

To address this uncertainty, we reconstruct regional atmospheric circulation in northwestern South America through the Plio-Pleistocene, an interval that includes the initiation of major Northern Hemisphere glaciation and long term cooling of the eastern equatorial Pacific cold tongue (Lawrence et al., 2006; Liu et al., 2019; Raymo, 1994; Tierney et al., 2019; Wara et al., 2005). We aim to constrain the sensitivities of atmospheric circulation in northwestern South America to various forcings using leaf wax biomarkers that track water isotopologues in precipitation, hereafter referred to as 'water isotopes'. Water isotopes in precipitation have been instrumental in reconstructing past hydroclimate and circulation (Bhattacharya et al., 2022; Dee et al., 2023).

Applying this approach in northwestern South America is complicated by the dynamic surface uplift of the Andes, which was episodic over the last 80 to 70 million years (Ma). From 15 Ma to the present, the subduction of the Carnegie Ridge has caused exhumation rates in the Western Cordillera of the Andes to increase (Margirier et al., 2023; Spikings et al., 2001, 2010; Spikings and Simpson, 2014; Villagómez and Spikings, 2013). The surface uplift of the Western Cordillera may have left an imprint on water isotopes in precipitation through Rayleigh distillation, where water isotopes become more depleted in deuterium as elevation increases and temperature decreases (Rowley and Garzione, 2007). Therefore, disentangling signals of surface uplift and atmospheric circulation in this region is challenging (Pérez-Angel et al., 2022).

We address the influence of elevation change on water isotopes in precipitation by analyzing the contemporary relationship between water isotopes in precipitation, elevation, and westerly winds from the Global Network of Isotopes in Precipitation (GNIP) (Aggarwal et al., 2007) and ERA5 (Hersbach et al., 2020) along western Ecuador. We also measure the hydrogen and carbon isotopic composition of leaf wax biomarkers, since the relative proportion of deuterium to protium in leaf waxes (δD_{wax}) tracks the hydrogen isotopic composition of meteoric waters (δD_p) (Sachse et al., 2012). We investigate the hypothesis that δD_{wax} at Ocean Drilling Project (ODP) 1239 captures variations in the intensity of westerly water vapor transport from the Eastern Pacific Warm Pool. Our findings identify a gradual increase in water vapor transport through the Plio-Pleistocene controlled by evolving mechanisms.

2. Methods

2.1. Contemporary δD_p from GNIP

We develop an interpretive framework for understanding variations in reconstructed δD_p through the Plio-Pleistocene using instrumental observations of water isotopes in precipitation from the GNIP database (Aggarwal et al., 2007). We retrieved all GNIP station data available in Ecuador using the Water Isotope System for Data Analysis, Visualization, and Electronic Retrieval in February 2023 (https://www.iaea.org/resources/nucleus-information-resources).

GNIP station data was filtered to retain observations that contained measurements of δD_p, precipitation amount, and received water vapor transport from the Pacific ('Pacific Domain' in Figure 1 of Garcia et al., 1998). We included the Amaluza station (2.6° S, 78.567° W) because it shares a similar precipitation regime to the rest of the stations in the 'Pacific Domain', despite being slightly outside of the the 'Pacific Domain' bounds. We applied an additional filter and retained stations with at least 12 consecutive observations (i.e. one year) to minimize the influence of precipitation seasonality (Pérez-Angel et al., 2022).

Several stations contained more than 12 consecutive observations. For these stations, we take the first $\lfloor \frac{N}{12} \rfloor \times 12$ observations, where N is the number of consecutive observations. For example, the Uzchurumi station had 26 months of continuous measurements from 5/1/1992 to 6/30/1994, of which we discarded the last two observations resulting in 24 consecutive observations. By discarding the last two observations, we prevent adding observations, and bias, to the dry season. This filtering procedure resulted in five stations situated along the Pacific coast of Ecuador spanning May 1992 through April 1994 (Table S1). This interval coincides with a low Niño 1+2 and 3.4 index and indicates neutral El Niño conditions during the measurement interval (Table S1).

Despite careful filtering and GNIP station selection, the short duration of the GNIP station adds uncertainties to our δD_p interpretation that are difficult to quantify, particularly for interannual variability in δD_p. However, interannual hydroclimate and westerly wind variability are well constrained for west Ecuador (Emck, 2007; Morán-Tejeda et al., 2016) and the eastern equatorial Pacific (Poveda et al., 2006) and our GNIP station reasonably match the long-term climatology of west Ecuador (Figure 1). We averaged δD_p for long-term monthly means weighted by precipitation amount. Weighting by

precipitation amount reduces the influence of months with little precipitation but anomalous measured δD_p values.

To identify the controls on δD_p in western Ecuador, we model the relationship between westerly winds directed towards western Ecuador, monthly precipitation, and monthly precipitation-weighted δD_p with a series of linear mixed-effects models. Our index of west Ecuadorian zonal wind strength is built upon the Choco jet index, but restricted to the latitudinal bounds of Ecuador. As in the Choco jet index, we take the maximum zonal wind averaged between 80-82° W at 925 hPa (Sierra et al., 2021), but limit the latitudinal range to 5°S-2°N, (versus 10°S to 10°N for the Choco jet index (Sierra et al., 2021)). This westerly wind index is well correlated with the Choco jet and broader westerly transport in the eastern equatorial Pacific across several pressure levels (Figure S1).

In our linear mixed-effects models, west Ecuador zonal wind intensity and monthly precipitation are fixed effects, elevation is a random effect, and δD_p is the response variable. We perform model selection by comparing all combinations of predictors and corresponding model diagnostics (e.g. Akaike's Information Criterion and log-likelihood). We also assess linear mixed-effects models where δD_p is cube-root transformed to more evenly weigh high and low elevation stations. High-elevation stations have larger changes in monthly δD_p and contribute more variability to the linear mixed-effects models. From these linear mixed-effects models, we report conditional and marginal R^2 which correspond to variance explained by random and fixed effects, respectively (Nakagawa and Schielzeth, 2013). Conclusions from linear mixed-effects models with transformed and untransformed monthly δD_p are largely similar except for the significance of the random effect term, so for simplicity, we present the untransformed results with all results in Table S2.

2.2. ODP Core 1239A

ODP1239 (0°40.32′ S, 82°4.86′ W) was cored in 2002 and is located ~120 km off the western coast of Ecuador, on the Carnegie Ridge at 1414 m water depth. The Pliocene portion of the sediment is predominantly pelagic and composed of olive gray nanofossil oozes with varying proportions of clay, diatoms, foraminifers, and micrite (Mix et al., 2003). The South Pacific Subtropical High creates southerly winds along the coast of Peru and Ecuador imparting easterly wind stress, upwelling the Equatorial Undercurrent, and developing the characteristic eastern equatorial Pacific cold tongue (Strub

et al., 1998). The extent of the cold tongue is greatest at the end of the austral winter and exposes ODP1239 to cool, nutrient-rich waters (Strub et al., 1998; Locarnini et al., 2013). This oceanographic setting changed very minimally during the Pliocene as ODP1239 migrated eastward alongside the Nazca plate towards Ecuador (Mix et al., 2003). From 6 Ma to present, ODP1239 migrated 2° (~200 km) eastward and 0.75° (~75 km) northward suggesting that leaf waxes sourced from western Ecuador for the duration of our reconstruction. Prior work at ODP1239 has indicated that sediment source is limited to the Western Cordillera of western Ecuador, particularly from the Guayas, Esmeraldas, and Cayapas rivers in Ecuador (Grimmer et al., 2018, 2020; Rincón-Martínez et al., 2010).

Age estimates from this core are based on biostratigraphy and orbital tuning from Timmermann et al. (2007) between 4.956 Ma and 2.7 Ma. For samples younger than 2.7 Ma, we use the age model from Etourneau et al. (2010) that is orbitally tuned. We had a single sample at 387.15 meters composite depth below seafloor (mcd) that was outside of either age model available at ODP1239 covering the interval of reconstructed δD_p. For this sample, we assigned the nearest constrained age of 4.956 Ma from Timmermann et al. (2007) at 385.43 mcd. This assigned age is likely ~20,000 years too young based on the average sedimentation rate at ODP1239 in the interval from 4.956 Ma to 2.7 Ma (Timmermann et al., 2007) but this age uncertainty does not influence any conclusions as we focus on the long-term trends in the record.

2.3. Leaf Wax Analyses

We reconstructed past changes in precipitation isotopes using leaf-wax biomarkers from terrestrial plants that incorporate meteoric waters into their tissues (Sauer et al., 2001; Sternberg, 1988). Leaf waxes are produced by higher terrestrial plants to prevent leaf desiccation and environmental damage (Eglinton and Hamilton, 1967). These compounds are transported into marine sediments by entrainment in wind or in fluvial sediments (Kusch et al., 2010) where they can be preserved in sedimentary archives over geologic timescales (years to millions of years). We analyzed C_{30} *n*-alkanoic acids because they are only produced by terrestrial plants (Kusch et al., 2010; Sachse et al., 2012) and are more abundant than C_{29} *n*-alkanes in ODP1239 sediments.

We followed standard analytical methods for extraction, quantification, and compound-specific isotope measurements of *n*-alkanoic acids (Bhattacharya

et al., 2018). Sediments were first lyophilized, homogenized, mixed with pre-combusted diatomaceous earth, and then extracted with a mixture of 9:1 dichloromethane:methanol in a Dionex Accelerated Solvent Extractor 350. A general recovery standard was added to the total lipid extracts to aid in quantification. Fatty acids were purified from the total lipid extracts with column chromatography. We used aminopropyl gel and eluted with 2:1 dichloromethane:isopropanol and 4% acetic acid in dichloromethane for the neutral and acid fractions, respectively. The purified acid fraction was methylated using methanol of known isotopic composition to form fatty acid methyl esters (FAME). FAMEs were further purified using 5% deactivated silica gel columns with 100% dichloromethane as an eluent. We quantified FAMEs using a TRACE1310 gas chromatograph equipped with a programmable temperature vaporizer inlet and flame ionization detector.

Measurements of δD_{wax} and $\delta^{13}C_{wax}$ were made using a similar TRACE1310 coupled to a Thermo Delta V Plus via a GC-Isolink II device. To monitor for instrument drift and normalize for any offsets, we measured a synthetic mix of FAMEs with a known isotopic value every 5 samples (Bhattacharya et al., 2022). Standard errors for isotopic value of the C_{28} fatty acid in our synthetic FAMEs are 0.053‰ ($\delta^{13}C$) and 0.28‰ (δD), indicating high measurement precision and accuracy after correcting for drift. Measurements were performed in quadruplicate to achieve a precision greater than 2‰ and 0.2‰ for δD_{wax} and $\delta^{13}C_{wax}$, respectively. We report values after applying mass balance corrections to account for the added methyl group from methylation.

2.4. δD_p reconstructions

A synthesis of C_{29} *n*-alkane plant leaf waxes preserved in surface sediments of lacustrine environments demonstrates a strong linear relationship between δD_{wax} and δD_p (Sachse et al., 2012). Sedimentation and leaf wax transport minimally influences this strong relationship. δD_{wax} in lacustrine sedimentary archives is highly correlated to δD_p (Sachse et al., 2004) and this linear relationship holds across precipitation, humidity, and vegetation gradients (Hou et al., 2008).

While evapotranspiration can enrich soil and leaf waters in the heavier isotope, influencing individual plants, the effects of evapotranspiration on wax isotopes may be small at an ecosystem scale (Ehleringer and Dawson, 1992; Feakins and Sessions, 2010). During wax synthesis in plants preferentially incorporate lighter isotopes of meteoric waters into their tissues, resulting in biosynthetic fractionation (ϵ_p) and δD_{wax}. Together, these processes result in

a wax molecule that is depleted in deuterium relative to source water δD_p by an 'apparent fractionation' or ϵ_p (Sessions et al., 1999). ϵ_p varies across plant life forms, which strongly correlates with photosynthetic pathway. C_3 shrubs and trees and C_4 graminoids represent two fractionation end members: C_3 plants have a smaller ϵ_p compared to graminoids (Gao et al., 2014; Smith and Freeman, 2006).

We leveraged this robust empirical relationship to reconstruct δD_p from measurements of δD_{wax} from ODP1239 in a Bayesian isotope mixing model following Tierney et al. (2017). In this framework, ϵ_p is modeled from measurements of $\delta^{13}C_{wax}$ and contemporary $\delta^{13}C$ from a global survey (Liu and An, 2020; Sachse et al., 2012). Once ϵ_p is determined, δD_p is reconstructed using Equation (1) (see Data Availability Statement, Bhattacharya et al., 2018, 2022; Tierney et al., 2017). Uncertainty in δD_{wax} measurements is propagated to reconstructed δD_p by randomly drawing samples from $\mathcal{N}(\mu_j, \sigma_j^2)$ for the ith sample from ODP1239 across j measurements of δD_{wax}.

$$\delta D_p = \frac{1000 + \delta D_{wax}}{\frac{\epsilon_p}{1000} + 1} - 1000 \tag{1}$$

Concentrations of FAMEs limited the amount of paired δD_{wax} and $\delta^{13}C_{wax}$ measurements. For low concentration samples, we prioritized measuring δD_{wax} and linearly interpolated $\delta^{13}C_{wax}$ to reconstruct δD_p within our Bayesian framework. Reconstructed δD_p is likely insensitive to linearly interpolating $\delta^{13}C_{wax}$ because $\delta^{13}C_{wax}$ never exceeds -27‰(Figure 2), suggesting that C_3 plants were the primary components of the leaf wax source pool and contributions from C_4 plants were likely small.

The contemporary and paleoecology of western Ecuador support this interpretation. The modern vegetation of western Ecuador is zonated by elevation and communities below the forest line (3,200 masl), such as the moist broadleaf forests and upper montane forests, are composed almost entirely of C_3 families and genera (Grimmer et al., 2018). C_4 plants become prominent in the Ecuadorian low elevation dry forests (Powell and Still, 2009) where the abundance of C_4 shrubs and grasses is controlled by precipitation amount (Grimmer et al., 2020). During the early and mid-Pliocene, fossil pollen abundances indicate that C_3 taxa were the primary vegetation components composing nearly half of all pollen deposited into ODP1239 (upper ,montane forest, lower montane forest, lowland rainforest, páramo in Grimmer et al., 2018, 2020), while C_4 taxa were only minor components that

rarely exceeded 10%. ϵ_p varies little among C_3 plants (Sachse et al., 2012), and various lines of evidence indicating an overwhelming abundance of C_3 plants in western Ecuador, presently and through the Plio-Pleistocene, suggests that ϵ_p likely changed minimally at ODP1239 over the last 5 Ma, which our isotope mixing-model captures (Figure S2).

2.5. Isotope-enabled Community Atmosphere Model simulations

We investigated the influence of equatorial Pacific SSTs on water isotopes in precipitation in northwestern South America with the isotope-enabled Community Atmospheric Model 5 (iCAM5 Brady et al., 2019; Knapp et al., 2022b). The simulation was initialized using SST fields from a Community Earth System Model version 1 simulation that best-captured proxy SST reconstructions in the equatorial Pacific from a series of perturbed cloud albedo simulations (Burls and Fedorov, 2014), particularly the reduced zonal temperature gradient of the early Pliocene (Knapp et al., 2022b).

The applied SST field coheres with Mg/Ca SST reconstructions that suggest a weakened zonal gradient in SSTs in the tropical Pacific before 3 Ma (i.e. permanent El-Niño configuration, Fedorov et al., 2006; Wara et al., 2005; White and Ravelo, 2020). However, SST reconstructions disagree in the western Pacific and yield conflicting interpretations of the zonal SST gradient in the tropical Pacific (Meinicke et al., 2021; Tierney et al., 2019; Wara et al., 2005; White and Ravelo, 2020; Zhang et al., 2014b). Alkenone and TEX_{86} reconstructions indicate higher temperatures than present in the western Pacific and do not support an inferred permanent El Niño-like configuration in the tropical Pacific, though alkenone reconstructions only extend to 4 Ma (Tierney et al., 2019; Zhang et al., 2014b).

Despite this disagreement in estimates of western SSTs in the Pliocene, there is agreement that the eastern equatorial Pacific cold tongue was much warmer than present (Herbert et al., 2016; Lawrence et al., 2006; Tierney et al., 2019; Zhang et al., 2014b). Our iCAM5 simulation includes this warming of the eastern Pacific which enables us to assess the influence of cold tongue warming on westerly low-level winds that influence hydroclimate in northwestern South America. The simulation was run with $0.9^\circ \times 1.25^\circ$ horizontal resolution and 30 vertical layers for 100 years, of which we average the last 50 years. Comparisons between the control iCAM5 simulation, observational GNIP station precipitation and δD_p, and ERA5 winds demonstrate that iCAM5 captures the broad features of hydroclimate in western Ecuador (Supplemental Information).

2.6. Eastern Equatorial Pacific sea surface temperature synthesis

We compared our leaf wax reconstructions to newly derived indices of Pacific SSTs. We compiled existing alkenone SST records that span the Plio-Pleistocene. The temperature gradient in this region of the eastern equatorial Pacific is closely related to mean sea-level pressure and Choco jet variability (Poveda and Mesa, 2000; Sierra et al., 2021). Five alkenone SST records in the eastern equatorial Pacific cold tongue span the interval for which we reconstruct δD_p: ODP1239 (Etourneau et al., 2010), ODP850 (Zhang et al., 2014b), ODP846 (Lawrence et al., 2006), Integrated Ocean Drilling Program site U1338 (Rousselle et al., 2013), and ODP847 (Figure 3, Dekens et al., 2007). ODP1241 (Seki et al., 2012) is outside of the influence of the eastern equatorial Pacific cold tongue and represents the off-equatorial region (Figure 3). We calibrated all records using BAYSPLINE (Tierney and Tingley, 2018) and propagated reconstruction errors to the gradient between the cold tongue to off-equatorial regions in the eastern equatorial Pacific with a Monte Carlo resampling approach (Tierney et al., 2019; Bhattacharya et al., 2022).

3. Results and Discussion

3.1. Interpretation of Isotopes

The seasonal climatology of δD_p along the Pacific coast of Ecuador is controlled by the intensity of westerly water vapor transport and precipitation amount, which is in turn modulated by elevation. GNIP δD_p in western Ecuador is low in MAM and progressively increases throughout the rest of the year (Figure 1D). Similarly, the westerly water vapor transport toward western Ecuador is weakest in MAM and increases to a maximum in SON, tracking the position of the Intertropical Convergent Zone (ITCZ) and convergent tropical easterly winds (Figure 1C, Sierra et al., 2021). When averaged across all GNIP sites, δD_p increases by ~39.86‰ following the strengthening of westerly winds in May (Figure 1D). This seasonal cycle is enhanced with elevation due to Rayleigh distillation. GNIP sites at higher elevations along the Western Cordillera exhibit the greatest seasonal change in δD_p. For instance, the lowest elevation GNIP station in western Ecuador that receives moisture transport from the Pacific (30 meters above sea level, masl) has an average δD_p increase of 27.78‰ when westerly winds begin to strengthen in May (Figure 1D). In contrast, the highest elevation station (1,720 masl) experiences a 83.93‰ increase from April to July (Figure 1D). This influence of elevation is moderately significant in our linear mixed-effects models

(Table S2) and is caused by Rayleigh distillation from temperature decreasing as elevation increases. A similar pattern is present in δD of river water in Ecuador where δD decreases as elevation increases, particularly along the Pacific coast of Ecuador (Gébelin et al., 2021).

The source of water vapor enriched in deuterium that increases δD_p when westerly winds are strong is likely the Eastern Pacific Warm Pool. Additional enrichment may occur as the result of processes like water vapor recycling (Salati et al., 1979) during transport toward western Ecuador. Water vapor isotopic composition measured from the Tropospheric Emission Spectrometer demonstrates that δD_{vapor} is highly enriched in deuterium in the Eastern Pacific Warm Pool (Figure S6). Westerly winds are strong over this region of water vapor enriched in deuterium and extend into western Ecuador (Figure 1A, S6). In MAM, this region of δD_{vapor} enriched in deuterium does not extend into western Ecuador, aligning with low δD_p at the GNIP stations (Figure S6). This spatial overlap explains the linear relationship between westerly winds and δD_p (Figure 1A). Stronger westerly winds transport more water vapor enriched in deuterium from the Eastern Pacific Warm Pool and increases δD_p in western Ecuador. Lagrangian trajectory analyses for the Pacific coast of Colombia also indicate the importance of Pacific water vapor sources in months when westerly winds are strongest (Hoyos et al., 2018; Sakamoto et al., 2011).

The precipitation amount effect that is commonly observed in tropical records of water isotopes in precipitation has a limited influence on δD_p along the Pacific coast of Ecuador. The precipitation amount effect is defined as the inverse relationship between the isotopic signature of precipitation and precipitation amount (Dansgaard, 1964). This relationship is thought to emerge, in part, because cooling rain clouds remove heavier isotopologues and rain drop re-evaporation decreases as humidity increases during precipitation (Dansgaard, 1964; Rozanski et al., 1993). From our linear mixed-effects models, we find that west Ecuador zonal wind strength is a stronger predictor of δD_p than monthly precipitation amount. When west Ecuador zonal wind strength is the only predictor, linear mixed-effects model fit is better than when precipitation amount is the only predictor (13.21 higher log-likelihood and 26.44 lower AIC, Table S2). This pattern holds when adding west Ecuador zonal wind strength and precipitation amount as secondary predictors. Monthly precipitation amount as an additional predictor to west Ecuador zonal wind strength only marginally improves linear mixed effect model fit (0.65 increase in log-likelihood but a 0.72 *increase* in AIC,

Table S2). In contrast, west Ecuador zonal wind strength as an additional predictor to monthly precipitation amount greatly improves linear mixed effect model fit (13.86 increase in log-likelihood, 27.72 decrease in AIC, Table S2). However, elsewhere in Ecuador, the amount effect does emerge. For example, the Espoch (2,820 masl), Quito-Inamhi (2,789 masl), and Cuenca (2,510 masl) GNIP stations appear to have a linear relationship between precipitation amount and δD_p (Garcia et al., 1998). Nevertheless, our linear mixed-effect models demonstrate that along the west coast of Ecuador water vapor sources overprint local amount effects. For these reasons, we find that δD_p on the west coast of Ecuador is primarily controlled by changes in westerly water vapor transport from the Eastern Pacific Warm Pool and that reconstructed δD_p at ODP1239 records changes in this transport during the Plio-Pleistocene.

3.2. δD_p trends at ODP1239

Reconstructed δD_p at ODP1239 exhibits a gradual increase with a decrease at ~3 Ma (Figure 2B). Reconstructed δD_p values in the earliest portion of the record (5.0 to 4.6 Ma) are among the most negative, averaging -8.85‰ and suggest weak westerly transport from the Eastern Pacific Warm Pool during the early Pliocene. After the early-Pliocene, δD_p increased by 5.16‰ into the mid-Piacenzian warm period (3.264 - 3.025 Ma) (Figure 3A) which indicates a strengthening of westerly transport of water vapor enriched in deuterium from the Eastern Pacific Warm Pool. A decrease of 7.30‰ from the mid-Piacenzian warm period to 2.7 Ma (200,000 year average centered on 2.7 Ma) is synchronous with large-scale changes in the Earth system (Figure 3C), after which δD_p increases by 5.52‰ and marks the end of the Pliocene. This decrease is coincident with the onset of major Northern Hemisphere glaciation (Raymo, 1994), though the exact timing of glaciation events remains debated. The Pleistocene section of ODP1239 mirrors the Pliocene with an overall increasing trend that is interrupted by an abrupt increase in δD_p of 9.30‰ from 1.7 to 1.6 Ma, synchronous with increases in SSTs of 1.65 and 0.42 °C in the eastern Pacific Cold tongue, as reconstructed from the alkenone paleothermometer at ODP1239 and ODP846, respectively (Figure S7, Etourneau et al., 2010; Lawrence et al., 2006; Seki et al., 2012). The relationship between variations in westerly water vapor transport and global to regional climate changes suggests potential controls on the dynamics that govern the position and strength of westerly transport.

A gradual increase of δD_p at ODP1239 suggests that changes in Andean topography were not the dominant controls on reconstructed δD_p through the Plio-Pleistocene. Evidence from thermochronological constraints (Spikings et al., 2001, 2010; Villagómez and Spikings, 2013), detrital zircon typology coupled with U/Pb geochronology (Osorio-Granada et al., 2017), provenance analyses (León et al., 2018), fossil pollen (Grimmer et al., 2018), and zircon geochronology (Echeverri et al., 2015) collectively suggest the presence of significant topography in the Western Cordillera by the late-Miocene/early-Pliocene. Notably, exhumation rates increase after 15 Ma from the subduction of the Carnegie Ridge (Margirier et al., 2023; Spikings et al., 2001; Spikings and Simpson, 2014).

Any surface uplift after 5 Ma would have imposed a negative trend because water isotopes in precipitation become depleted in deuterium as elevation increases (Figure 1, Ambach et al., 1968). This relationship holds in western Ecuador where the elevation random effect in our linear mixed-effects models is moderately significant regardless of the predictors included in the models (Table S2). When δD_p is cube-root transformed the elevation random effect is statistically insignificant, as the transformation selectively reduces δD_p variability in regions with substantial fluctuations (i.e. high elevations). This reaffirms the crucial role of elevation on δD_p patterns in western Ecuador caused by Rayleigh distillation (Table S2). Elevation also emerges as an important control on river-based δD (Gébelin et al., 2021). Nevertheless, δD_p at ODP1239 exhibits gradual increase, indicating that another factor, such as water vapor transport, opposes and overwhelms any potential change in δD_p due to elevation.

Leaf wax sources into ODP1239 may contribute to the minimal influence of elevation in reconstructed δD_p. δD_{wax} is likely primarily sourced from the Guayas, Esmeraldas, and Cayapas rivers in western Ecuador because prevailing winds in western Ecuador are westerly (Figure 1E, S3A). River discharge from the Guayas and Esmeraldas Rivers are unimodal and mirror precipitation in coastal Ecuador (Rincón-Martínez et al., 2010). Therefore, δD_{wax} inputs into ODP1239 may be biased towards the western Ecuadorian lowlands and may partly explain the small influence of elevation in reconstructed δD_p. Whether this bias is present does not influence our conclusion that reconstructed δD_p primarily reflects changes in water vapor transport, making δD_{wax} an unreliable proxy of elevation in this setting.

3.3. Westerly moisture transport variability and hydroclimate changes during the Pliocene

Variations in westerly water vapor transport during the Plio-Pleistocene are associated with changed hydroclimate and ecological turnover in western Ecuador through a coupling with the South Pacific Subtropical High. Today, when westerly winds and the Choco jet are strong, precipitation increases in Colombia and decreases in Peru/Chile (Figure 3E), since westerly winds form in part from winds on the eastern edge of the South Pacific Subtropical High (Sierra et al., 2021). In the seasonal cycle westerly transport and the South Pacific Subtropical High are all strongest in SON (Figure S3A, Fahad et al., 2021). A strong South Pacific Subtropical High transports more moisture northward from the Pacific and associated subsidence dries Chile (Barrett and Hameed, 2017; Quintana and Aceituno, 2012). In MAM, the west Ecuadorian zonal winds, the Choco jet, and South Pacific Subtropical High are weak (Figure S3A, Fahad et al., 2021). A weakened South Pacific Subtropical High reduces subsidence over Chile/Peru and increases precipitation (Barrett and Hameed, 2017; Quintana and Aceituno, 2012). Based on this relationship, a weakened subtropical high would have weakened westerly water vapor transport during the early Pliocene (Figure 3C), decreasing precipitation in western Colombia and increasing rainfall in western Peru/Chile (Figure 3E).

iCAM5 simulations for the early Pliocene are consistent with these expectations. Positive precipitation anomalies in Chile and Peru are matched with negative precipitation anomalies in western Colombia and a decrease in the strength of the South Pacific Subtropical High (Figure 4B). High stream erosion and incision in the Atacama Desert support high inferred precipitation in the early Pliocene in Chile (Amundson et al., 2012; Hartley and Chong, 2002). This geomorphic evidence also points to brief periods of "extreme" precipitation following the mid-Pliocene drying of the Atacama Desert (Amundson et al., 2012). A decrease in δD_p at ODP1239 at the start of the Pleistocene (Figure 3C, E) suggests a brief interval of weakening in the South Pacific Subtropical High that could produce the conditions necessary for "extreme" precipitation in the Atacama Desert.

Ecological turnover inferred from fossil pollen in the early Pliocene at ODP1239 highlights the role that long-term changes in regional atmospheric circulation can have on ecosystem structure. Reduced westerly water vapor transport toward Ecuador during the early Pliocene (Figure 3A) is associated with a high abundance of taxa such as Cyperaceae and Ilex that gen-

erally prefer wetter climates (Figure 3D, Grimmer et al., 2018; Marchant et al., 2002). As westerly water vapor transport increased during the mid-Pliocene these taxa declined in abundance (Figure 3A, D). An indicator of lowland drying, Amaranthaceae prefers drier coastal environments and is in low abundance until the mid-Pliocene (Figure 3D, Grimmer et al., 2020). The shared decline in taxa that prefer humid conditions, an increase in Amaranthaceae, and an increase in westerly water vapor transport are consistent with interannual variations in precipitation in western Ecuador. In the present-day, El Niño events increase precipitation in western Ecuador (Morán-Tejeda et al., 2016) and weaken westerly water vapor transport (Poveda et al., 2006). Hence, weakened westerly water vapor transport in the early Pliocene may be linked to increased precipitation in the western Ecuadorian lowlands, supporting taxa that prefer humid conditions (Figure 3A, E Grimmer et al., 2018). Accordingly, a strengthening of westerly water vapor transport in the mid-Pliocene would be paired with precipitation decrease in the western Ecuadorian lowlands, enabling Amaranthaceae to expand (Figure 3A, E, Grimmer et al., 2020).

Fossil pollen from ODP1239 is assumed to be mostly fluvially sourced from the Cayapas, Esmeraldas, and Guayas Rivers (Grimmer et al., 2018, 2020), but eolian deposits are likely also an important contributor (Heusser and Shackleton, 1994). Winds along the Pacific coast of South America are predominantly from Chile (Strub et al., 1998) where conditions were wetter during the early Pliocene (Amundson et al., 2012; Hartley and Chong, 2002) and may have contributed to the high abundance of taxa that prefer humid conditions at ODP1239. Nevertheless, hypothesized precipitation changes in western Ecuador require further testing because the relationship between westerly winds/Choco jet and annual precipitation is weak (Figure 3E). Moreover, pollen may be responding to localized coastal convection in western Ecuador, while isotopes reflect large-scale changes in vapor transport. Long distance pollen dispersal may further confound pollen-based climate interpretations. More records are needed to establish spatial patterns of precipitation changes in northwestern South America during the Pliocene.

3.4. Evolving controls on atmospheric circulation through the Plio-Pleistocene

Atmospheric circulation in northwestern South America responded to evolving controls through the Plio-Pleistocene, with two regimes separated by the initiation of major Northern Hemisphere glaciation. SSTs in the eastern equatorial Pacific emerge as an important control on the westerly transport

of water vapor enriched in deuterium toward northwestern South America through the Pliocene. At present, the cold tongue to off-equatorial pressure and temperature gradients in the eastern Pacific drive interannual variability in the Choco jet (Sierra et al., 2021) and westerly winds that influence hydroclimate in western Ecuador (Rossel and Cadier, 2009). Across the Pliocene, SSTs between the cold tongue and off-equatorial regions evolved asymmetrically (Figure 3B, S7D-H). The difference in SSTs between the eastern equatorial Pacific cold tongue and ODP1241 (5°50.57′ N, 86°26.68′W), in the Eastern Pacific Warm Pool, is at a minimum during the early Pliocene and increases to present (Figure 3B). This configuration of SSTs would produce a low mean sea level pressure gradient (Lindzen and Nigam, 1987) and weak westerly winds, consistent with low δD_p.

A similar process occurs during modern El Niño events that force the Choco jet and westerly winds to weaken as the cold tongue warms and the mean sea level pressure gradient decreases from the cold tongue to the off-equatorial eastern Pacific (Poveda et al., 2006). After ~3 Ma a regional shoaling of the thermocline cooled the cold tongue more than regions to the north near the Warm Pool(Ford et al., 2015) (Figure 3). Accordingly, as the SST gradient from the eastern equatorial Pacific cold tongue to ODP1241 increases in the mid- to late-Pliocene, so too does δD_p. A larger SST gradient would have increased westerly transport of δD_{vapor} enriched in deuterium from the Eastern Pacific Warm Pool increasing δD_p at ODP1239 (Figure 3A,B, S7D-H).

A decline in westerly water vapor transport at ~3 Ma points to an increasing influence of high latitude forcings. The inception of major Northern Hemisphere glaciation (Raymo, 1994) would have altered global energy budgets as the Northern Hemisphere cooled more than the Southern Hemisphere from expansive ice sheets (Chiang and Bitz, 2005). Interhemispheric energetic imbalances imposed by the addition of ice in the Northern Hemisphere shift the ITCZ southward towards the equator in climate simulations, from its mean position in the Northern Hemisphere (Chiang et al., 2003; Chiang and Bitz, 2005; Schneider et al., 2014). The westerly winds that flow toward northwestern South America develop from southerly winds which follow the low mean sea level pressure of the ITCZ and are deflected eastward by Coriolis acceleration which changes direction across the equator (Sierra et al., 2021).

Shifting the ITCZ southward from the inception of major Northern Hemisphere glaciation would reduce Coriolis acceleration acting on southerly cross

equatorial winds, in turn reducing the westerly flow into northwestern South America. An ITCZ shift is supported by salinity data: sea surface salinity reconstructions from $\delta^{18}O_{salinity}$ at ODP1241 demonstrate a decline of 0.77 ‰ at 2.95 Ma, consistent with a southward shift in the ITCZ. This salinity drop is synchronous with reduced westerly water vapor transport, after which freshening accelerates (Figure 3A,C). $\delta^{18}O_{salinity}$ at ODP1241 begins to indicate freshening at 3.7 Ma suggesting the connection between Northern Hemisphere cooling, ITCZ position, and westerly wind strength in the eastern equatorial Pacific is complex.

The apparent decoupling between the ITCZ, westerly winds, and salinity at ODP1241 before 3.7 Ma may, partly, be the result of the exchange of water vapor between the eastern equatorial Pacific and the Caribbean. Topography was low during the formation of the Isthmus of Panama, with periods of water mass exchange as recent as 2.58 Ma (Groeneveld et al., 2014), and was likely lower still during the early Pliocene. The Isthmus of Panama has undergone continuous uplift since ~6 Ma (O'Dea et al., 2016) indicating that topographic barriers to water vapor transport from the Atlantic Ocean to the Pacific Ocean were low in the early Pliocene, possibly obscuring the relationship between ITCZ position and precipitation isotopes early in the ODP1239 record. Grain size analyses from ODP848 and ODP849, support an inferred shift of the ITCZ at 3 Ma from $\delta^{18}O_{salinity}$. Mean grain size increases briefly around 3 Ma suggesting stronger easterlies near the equator consistent with idealized climate model experiments that place a large ice sheet in the Northern Hemisphere (Broccoli et al., 2006).

3.5. Paired δD_p, Choco jet, and westerly water vapor transport changes in iCAM5

Our early Pliocene-like iCAM5 simulations support our hypothesized link between changes in the cold tongue to off-equatorial SST gradient in the eastern Pacific and westerly wind strength. The model is forced with a small tropical Pacific SST gradient (meridional and zonal) that forces a decrease in δD_p, which coheres with the direction of the signal at ODP1239. The magnitude of δD_p decrease in iCAM5 is smaller than reconstructed δD_p at ODP1239 for the early Pliocene and consistent with prior proxy-model comparisons (Figure 2B, 4). Generally, isotope-enabled climate models reproduce a smaller isotopic change than shown by proxies (Hu et al., 2018). δD_p decrease in iCAM5 is likely driven by circulation changes, since the model

simulates weakened westerly water vapor transport in the core Choco jet region and western Ecuador (Figure 4A). A reduction in westerly wind strength is greatest in JJA and SON (Figure S8) when the Choco jet and westerly water vapor transport is at its climatological maximum (Figure S3). Furthermore, simulated precipitation changes are not spatially coherent with δD_p in northwestern South America, suggesting that δD_p fluctuations are not caused by precipitation amount in iCAM5 (Figure 4C, D). We hypothesize that upstream changes in δD_p in iCAM5 helps decrease δD_p in western Ecuador. iCAM5 has an inverse linear relationship between stratiform rainfall amount and precipitation isotopes (Hu et al., 2018). The proportion of stratiform rainfall increases in the central tropical Pacific which decreases δD_p. Integrated water vapor transport anomalies show greater transport from the central tropical Pacific where δD_p decreases and stratiform rainfall fraction increases are greatest (Figure 5).

Reduced regional and basin-wide SST gradients in the tropical Pacific force a weakening of the Choco jet and westerly winds towards the northwestern South America in iCAM5. Our prescribed SST fields in our iCAM5 simulation are mostly unchanged from the control simulation in the western Pacific, but are much higher in the eastern Pacific, resembling a permanent El Niño-like climate state (Knapp et al., 2022b). A low zonal SST gradient in the tropical Pacific may also explain weaker westerly winds in the eastern equatorial Pacific (Figure 4) on top of the influence of the cold tongue/off-equatorial gradient of temperature in the eastern equatorial Pacific. A low zonal SST gradient in the tropical Pacific weakens the Walker Circulation and lowers mean sea level pressure over the eastern Pacific (Bjerknes, 1969). Westerly winds towards northwestern South America are partly driven by high mean sea level pressure over the eastern equatorial cold tongue (Poveda and Mesa, 2000; Poveda et al., 2014; Sierra et al., 2018). These winds would weaken as mean sea level pressures fall in the eastern Pacific. Hence, a low zonal SST gradient in the tropical Pacific and a permanent El Niño-like state are consistent with weakened westerly transport inferred at ODP1239 in the early Pliocene (Figure 3A).

Our results suggest that northwestern South America is strongly sensitive to alternative configurations of tropical Pacific temperature gradients in isotope-enabled climate models. Basin-wide zonal and meridional SST gradients in the Pacific contribute to establishing global atmospheric circulation and climate patterns. Reconstructing these spatial gradients through the Plio-Pleistocene has received considerable attention using estimates of SST

(Fedorov et al., 2015; Tierney et al., 2019; Wara et al., 2005; Zhang et al., 2014a) but proxies sensitive to atmospheric circulation are underutilized. In northwestern South America, modern and past variations in westerly winds respond to regional (e.g. cold tongue to off-equatorial) and basin-wide (e.g. western to eastern Pacific) SST gradients in the tropical Pacific (Poveda and Mesa, 2000; Sierra et al., 2021). In turn, westerly water vapor transport controls δD_p in northwestern South America. Our findings suggest that records of δD_p in northwestern South America are an important benchmark for constraining the evolution of SSTs and atmospheric circulation across the tropical Pacific.

4. Conclusions

Westerly winds are a key feature of atmospheric circulation in northwestern South America, particularly those concentrated in the Choco jet (Poveda and Mesa, 2000). Climate models (Sierra et al., 2021) and proxy reconstructions (Martínez et al., 2003) demonstrate the sensitivity of winds in this region to the background climate state, but proxy evidence for greenhouse climate states has been sparse.We presented a new record of δD_p from ODP1239 reconstructed from C_{30} *n*-alkanoic acids that span the Pliocene and Pleistocene to address this uncertainty. Our analysis of observational δD_p from GNIP stations in western Ecuador demonstrates westerly winds in the eastern equatorial Pacific transport water vapor enriched in deuterium from the Eastern Pacific Warm Pool (Figure 1, S6). When westerly winds are weakest, δD_p is low in western Ecuador, and only begin to increase as westerly winds strengthen in May transporting water vapor enriched in deuterium. Applying this contemporary relationship to reconstructed δD_p from ODP1239 suggests that westerly winds were weak during the early Pliocene and gradually strengthened to the present. Changes in the equatorial cold tongue to off-equatorial SST gradient in the eastern Pacific drive changes in these westerly winds, and this gradient was at a minimum in the early Pliocene. In an early Pliocene iCAM5 simulation, δD_p decreases in northwestern South America from a weakening of westerly water vapor transport and increased transport of water vapor depleted in deuterium from upstream sources.

A gradual increase in δD_p through the Pliocene indicates that changes in water vapor sources overprint any signal of Ecuadorian Andean surface uplift on δD_p. Gradual increase is interrupted by a decrease at ~3 Ma, coincident

with the onset of major Northern Hemisphere cooling (Raymo, 1994). We hypothesize that this decrease is caused by extratropically-forced shifts in the configuration of the Southern Hemisphere Hadley Cell and the ITCZ. A similar mechanism could have operated on glacial/interglacial timescales but requires higher resolution records to test this hypothesis. The weakening of westerly water vapor transport in response to decreases in regional SST and mean sea level pressure gradients that emerge in our proxy-model comparison agrees with projected changes to the Choco jet by the end of the 21st century. Under high emission scenarios, projections demonstrate a weakening and southward shift of the Choco jet as the mean sea level pressure gradient between the eastern Pacific cold tongue and northwestern South America decreases (Sierra et al., 2021), with implications for regional ecosystems, biodiversity, and hydroclimate-related risks.

4.1. Acknowledgements

TB acknowledges funding from NSF P2C2 award OCE-2103015. RF acknowledges funding from NSF P2C2 award OCE-2103055. NJB and SK acknowledge funding support from NSF Award AGS-1844380. LPA acknowledges funding support from NSF award SGP 1929199. We thank the Integrated Ocean Drilling Program, especially the Gulf Coast Repository, for providing the sediment for site 1239. Discussions with Claire Rubbelke, Peter Brennan, Helbert Schneider Garcia Delgado, and Stephanie Bullinger greatly improved the manuscript and visualizations. The PaleoX seminar series provided great feedback and support throughout the development of this manuscript. We thank two anonymous reviewers for their feedback, which greatly improved the manuscript.

4.2. Data Availability Statement

All data and code used in this study are available on Zenodo (Fastovich et al., 2023). The new δD_p record for ODP1239 is also available on the NOAA NCEI Paleoclimatology database. iCAM5 results are available on Zenodo (Knapp et al., 2022a).

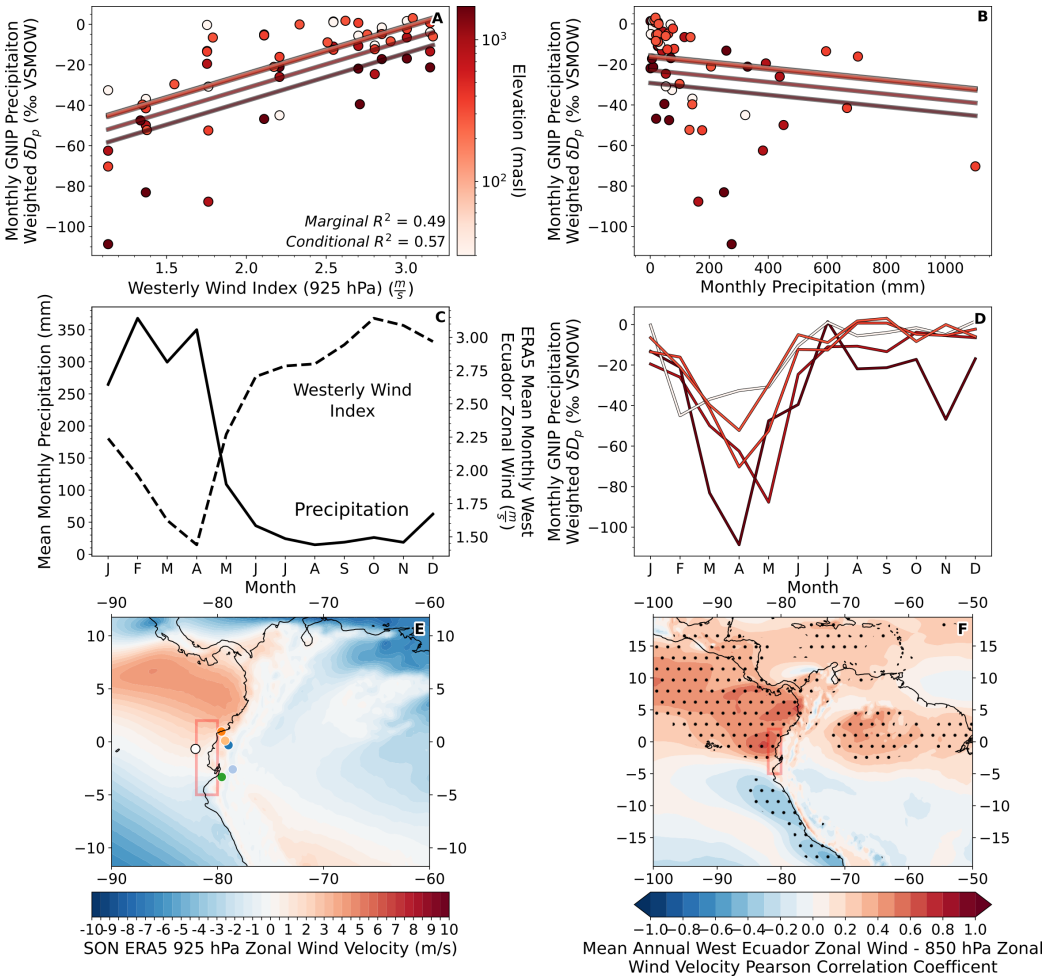

Figure 1: The linear relationship between monthly averaged δD_p from GNIP stations, (A) westerly wind strength index, and (B) monthly precipitation. The lines correspond to the station-level fit (i.e. including fixed and random effects) of a linear mixed-effect model with west Ecuador zonal wind and monthly precipitation amount as predictors and elevation as a random variable (model 2 in Table S2). Colors correspond to GNIP station elevation. (C) Monthly averaged precipitation from GNIP stations in west Ecuador and west Ecuador zonal wind intensity. (D) The monthly climatology of δD_p from all GNIP stations colored by elevation, as in (A) and (B). (E) The SON climatology of 925 hPa zonal winds from ERA5 between the period 1959 and 2022 with GNIP stations marked as points. ODP1239 is located off the coast of Ecuador and is labeled by a white point. (F) The correlation between west Ecuador zonal wind and 850 hPa zonal winds from ERA5. Stippling indicates significance at the 95% confidence level based on a Student's t-test. The red box denotes the region used when calculating the westerly wind strength index. Note, all δD_p averages are precipitation weighted. The legend for (E) is located in Table S1.

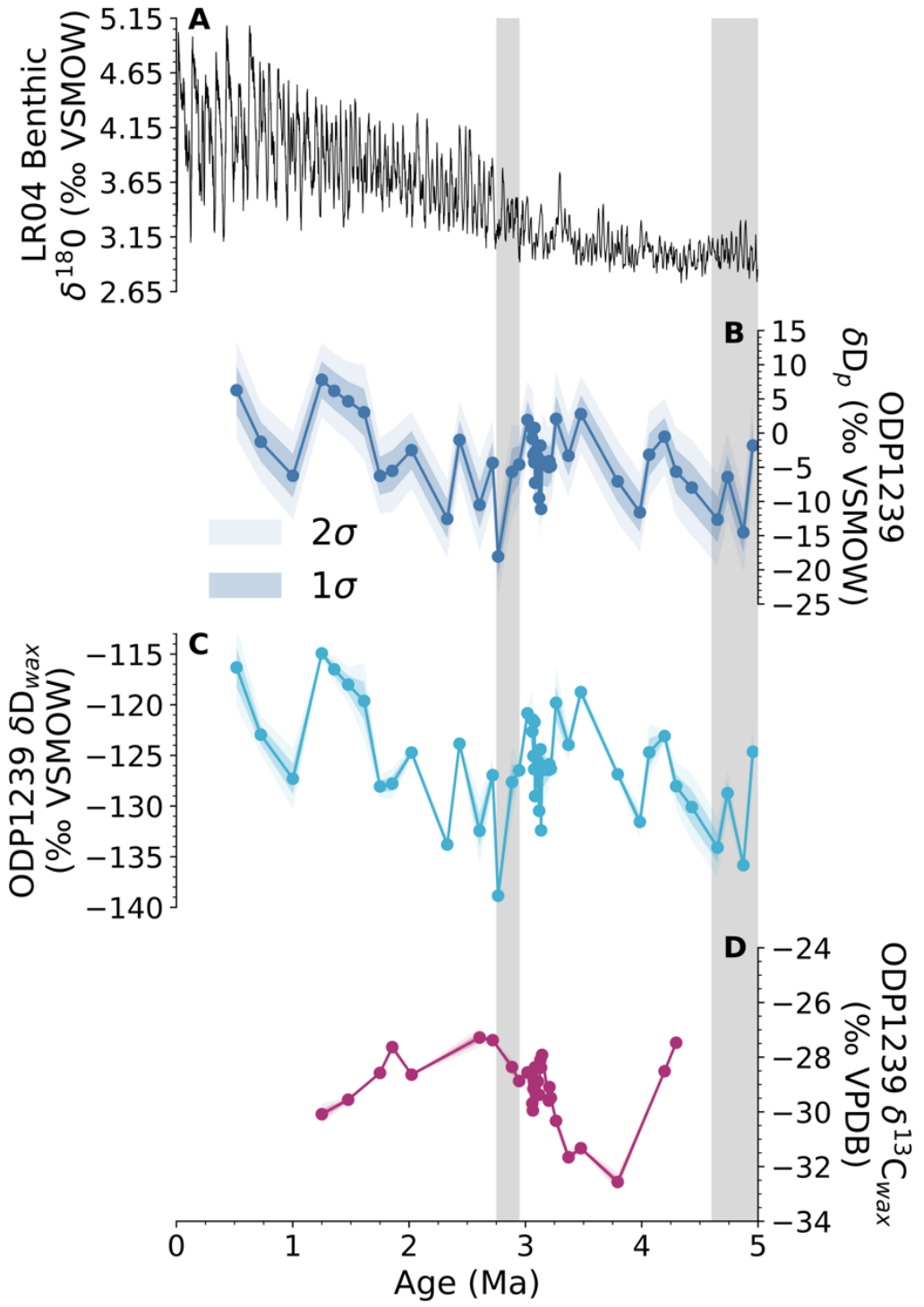

Figure 2: (A) Globally averaged benthic foraminifer δ^{18}O (Lisiecki and Raymo, 2005). (B) Reconstructed δD_p at ODP1239. (C, D) Measured δD_{wax} and $\delta^{13}C_{wax}$ from C_{30} *n*-alkanoic acids at ODP1239. The shaded area corresponds to the early Pliocene (5.0 to 4.6 Ma) and the onset of major Northern Hemisphere glaciation (3.0 to 2.75 Ma).

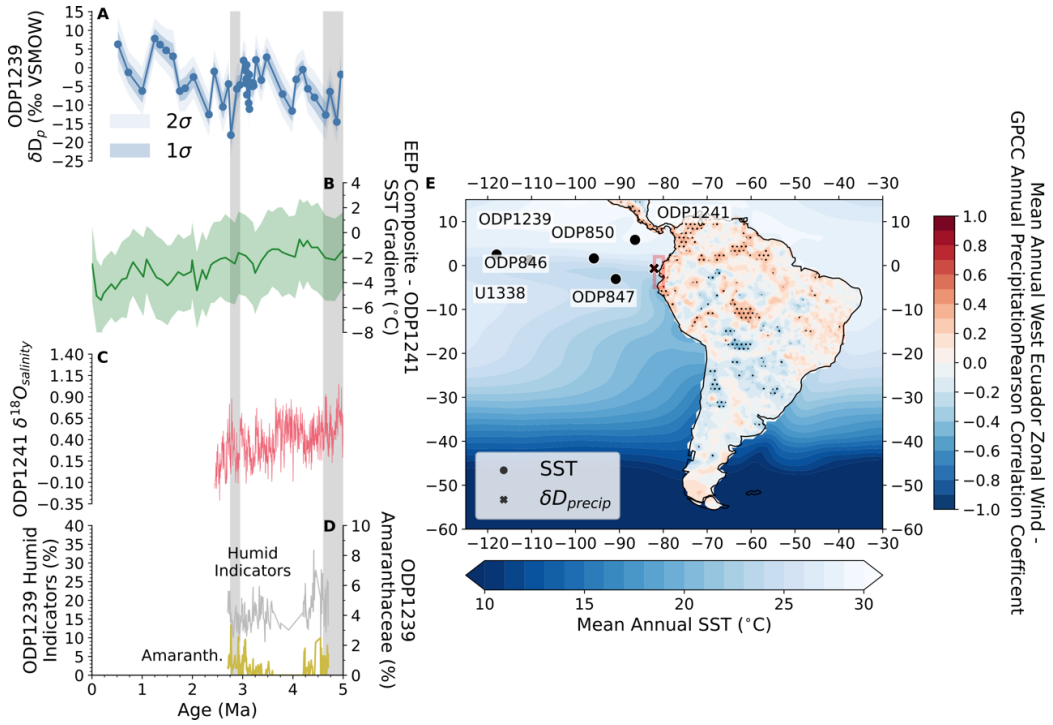

Figure 3: (A) Reconstructed δD_p at ODP1239. (B) The SST gradient between the eastern equatorial Pacific cold tongue composite and ODP1241 which has a close correspondence to Choco jet strength (Sierra et al., 2021). (C) Reconstructed sea surface salinity based on $\delta^{18}O$ from ODP1231 that serves as a record of ITCZ position (Groeneveld, 2005). (D) Fossil pollen-based indicators of humidity and aridity (Amaranthaceae) at ODP1239 as percent abundance (Grimmer et al., 2018, 2020). The shaded area corresponds to the early Pliocene (5.0 to 4.6 Ma) and the onset of major Northern Hemisphere glaciation (3.0 to 2.75 Ma). (E) For South America, the color corresponds to the Pearson correlation coefficient between the westerly wind strength index and annual precipitation from the Global Precipitation Climatology Centre (GPCC) (Schneider et al., 2011) between the period 1959 and 2022. Stippling indicates significance at the 95% confidence level based on a Student's t-test. For oceans, the shading corresponds to the mean annual SST averaged between 1891 and 2023 from the COBE-SST data product (Ishii et al., 2005). The red box correspond to the region used to calculate the westerly wind strength index.

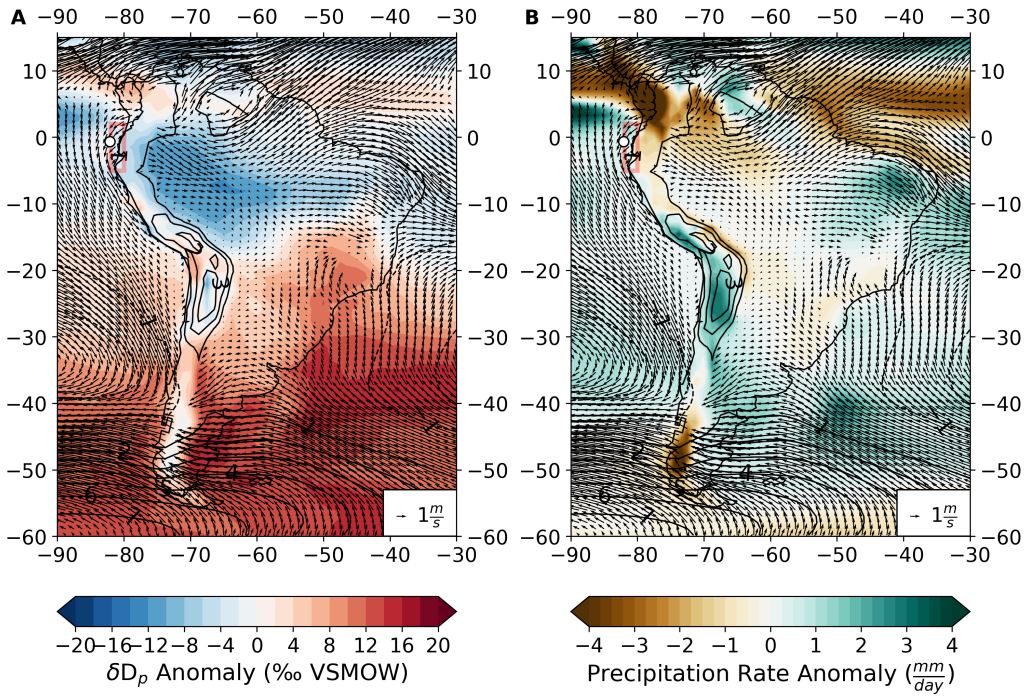

Figure 4: Annual climatological anomalies (early Pliocene experiment - control) from iCAM5 (Knapp et al., 2022b) for (A) δD_p and (B) precipitation rate forced with a reduced tropical Pacific zonal SST gradient. Contours represent mean annual sea level pressure anomalies with the zero contour omitted. Vectors correspond to wind anomalies at 925 hPa, where the Choco jet core is found (Poveda and Mesa, 2000; Sierra et al., 2021). ODP1239 is located off the coast of Ecuador and is labeled by a white point. The red box corresponds to the region used to calculate the west Ecuadorian zonal wind strength.

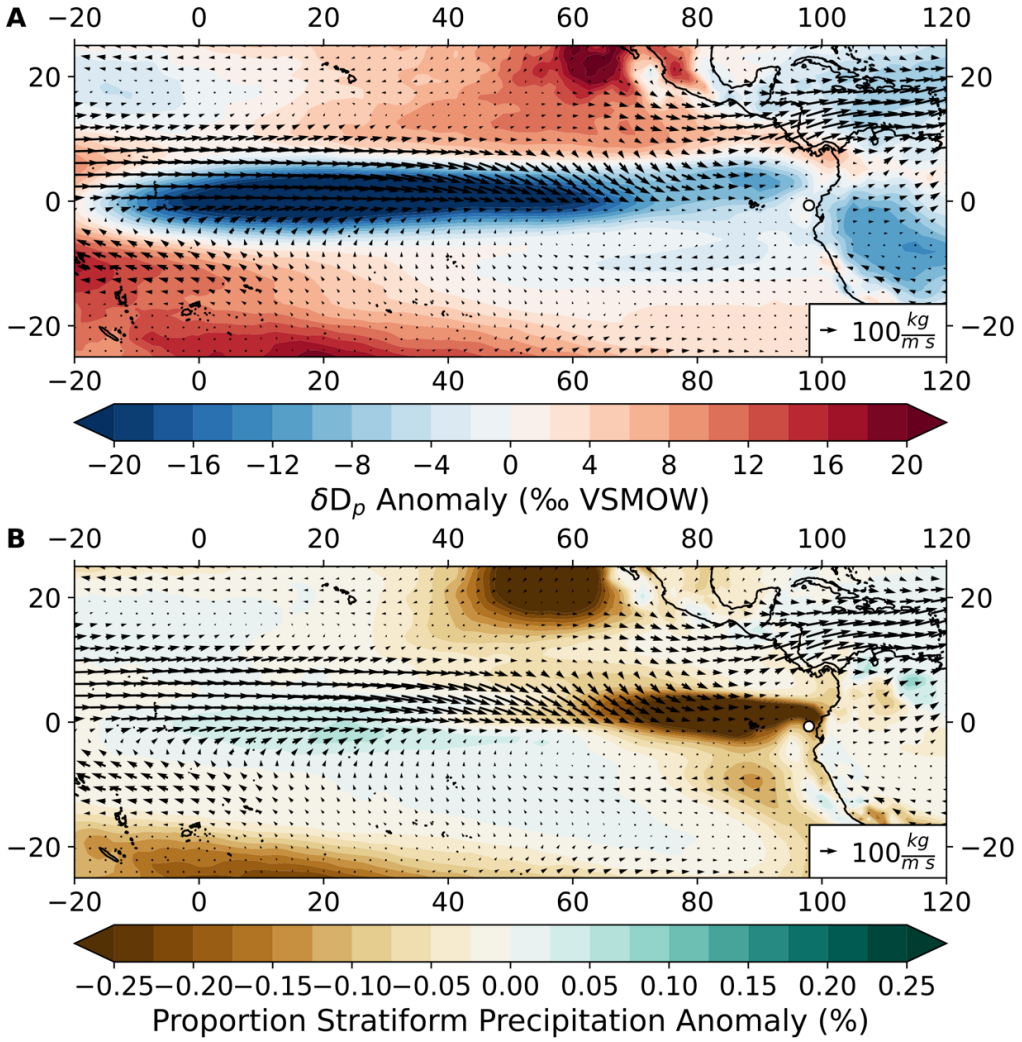

Figure 5: Simulated (A) δD_p and (B) proportion stratiform rainfall anomalies from iCAM5 (early Pliocene experiment - control, Knapp et al., 2022b). Vectors in (A) and (B) correspond to integrated water vapor transport anomalies from the surface to 200 hPa calculated using $\frac{1}{g}\int_{surf}^{200} q\mathbf{V}\,dp$, where g is gravitational acceleration, q is specific humidity, and the vector $\mathbf{V}$ represents the meridional and zonal components of wind.

5. Supplemental Information

5.1. Control iCAM5 simulation performance

The control simulation of iCAM5 captures the seasonal climatology of precipitation, water isotopes in precipitation, and the westerly winds in northwestern South America. Westerly wind strength increases beginning in May and reaches a maximum in September-October-November (SON), after which it declines to a minimum in March-April-May (MAM), as in ERA5 (Figure S3). Alongside the seasonal variability of the westerly winds, iCAM5 captures the northward migration of westerly winds which are at their most northern extent in SON (Figure S3). Although iCAM5 captures the broad patterns of the contemporary westerly winds well, 925 hPa zonal winds are stronger than estimates from ERA5 (Figure S3).

Monthly variations in δD_p are also captured in the control simulation. GNIP station δD_p in western Ecuador is largest in December-January-February (DJF), June-July-August (JJA), and SON (-11‰) and smallest in MAM (-55‰, Figure S4). Simulated δD_p is also at a minimum in MAM (-69‰) and a maximum in June-October (-25‰) (Figure S4). However, iCAM5 does not completely capture the monthly δD_p cycle observed at the GNIP stations. Low δD_p at the GNIP stations is limited to MAM while iCAM5 extends this interval of low δD_p from November to March which causes iCAM5 to be biased low by 25‰, when averaged across all months (Figure 1D, S3A). Limiting this comparison to MAM and June-October, this negative bias in iCAM5 is reduced to 14‰. Collectively, this data-model comparison demonstrates that iCAM5 reasonably captures monthly patterns in δD_p at the GNIP stations, albeit with imperfect timing.

iCAM5 demonstrates moderate accuracy simulating precipitation patterns in Ecuador, which vary with elevation. The lowlands receive 1,500 to 3,000 mm of rainfall annually, with a single wet season from January to April (Garcia et al., 1998; Morán-Tejeda et al., 2016). In the Ecuadorian Andes, total precipitation decreases to 500 to 1,500 mm of rainfall annually with two wet seasons from March-May and October-November (Garcia et al., 1998; Morán-Tejeda et al., 2016). The $0.9° \times 1.25°$ horizontal resolution of iCAM5 precludes the model from capturing these local elevation effects entirely, but iCAM5 demonstrates some success. Near the Pacific coast simulated precipitation is unimodal with the greatest precipitation from January to May and a pronounced dry season from June to September (Figure S4). At higher elevations, precipitation reaches a maximum in February, decreases to a minimum

in July, and begins to increase steadily after September in iCAM5 (Figure S5B).

The inability of iCAM5 to accurately simulate the bimodal precipitation at high elevations in Ecuador highlights different processes that control simulated precipitation and δD_p. Water vapor transport toward western Ecuador is controlled by large scale atmospheric circulation features, such as the position of the ITCZ, (Rossel and Cadier, 2009) which iCAM5 captures reasonably well as indicated by agreement between simulated 925 hPa winds and observations from ERA5 (Figure S3). However, at higher elevations water vapor transport and precipitation are linked topography (Garcia et al., 1998) which is a challenge in iCAM5 because of coarse horizontal resolution. Closer agreement between simulated and GNIP δD_p than simulated and GNIP precipitation suggests that δD_p in western Ecuador is likely controlled by water vapor transport, for which iCAM5 is well suited to investigate.

5.2. Controls on leaf wax hydrogen isotopes

Leaf waxes are a group of compounds produced by plants to protect from leaves from dessication. Plants uptake meteoric water for photosynthesis and incorporate the hydrogen isotopic composition of meteoric waters (δD_p) into their tissues. Leaf waxes are long chain *n*-alkyl lipids that are resistant to modification in geologic archives (Inglis et al., 2022).

Before leaf wax biosynthesis, soil water enrichment and leaf water transpiration can influence the hydrogen isoptic signature of meteoric waters encoded in leaf waxes. In the arid environments of southern California, where soil water evaporation rates are high, there is little difference between δD of ground water (source from rainfall) and the δD_p of xylem water (Feakins and Sessions, 2010). This close correspondence indicates that soil water evaporation and subsequent increase in δD does not influence the isotopic signature of water taken up by plants and δD_{wax}, since plants may preferentially use less evaporated sources of water like groundwater (Feakins and Sessions, 2010). Transpiration causes $\delta D_{leaf\ water}$ to be higher than δD_p and the magnitude of this increase varies with species, sampling time, and climatological paramaters (Feakins and Sessions, 2010). Fractionation during biosynthesis of leaf waxes decreases δD_{wax} relative to source $\delta D_{leaf\ water}$ and $\delta D_{xylem\ water}$. Collectively, these three processes result in an apparent fractionation (ϵ_p) between δD_{wax} and δD_p that seems relatively constant across ecosystem types ranging from arid to humid (Ehleringer and Dawson, 1992).

However, ϵ_p appears sensitive to plant functional type possibly because of differential leaf architecture, the differential use of intermediate photosynthetic products and the timing of leaf wax production (Sachse et al., 2012). However, ϵ_p is remarkably stable across environments for ecosystems that share common plant functional types. Forests comprised of C_3 dicotyledonous trees in Ecuador, Nicaragua, and Pennsylvania share an ϵ_p of ~120‰, including trees that are evergreen, semi-evergreen, and decidious (Polissar and Freeman, 2010). Forests in the Amazon have exceptional species and functional diversity for plants and yet ϵ_p from the tropical rain forest in Amazon lowlands to tropical montane cloud forests is also near ~120‰, despite environmental gradients in temperature and elevation (Feakins et al., 2016). High stability in ϵ_p across environments and ecosystems is reflected in the strong linear relationship between δD_{wax} and δD_p in global surveys (Sachse et al., 2012).

Reconstructing δD_p from geologic archives requires knowing ϵ_p of the ecosystem that formed the measured leaf wax lipids. If vegetation change is minor and only one plant functional type synthesized the measured leaf waxes for the entire geologic archive, then ϵ_p may be assumed constant. In this circumstance, contemporary measurements of ϵ_p (Sachse et al., 2012) across species and plant functional types can applied to correct for fractionation and reconstruct δD_p. However, this assumption rarely, if ever, holds since biotic and abiotic forces drive vegetation turnover through time. Therefore, reconstructing δD_p from δD_{wax} first requires estimating ϵ_p through time in a way that accounts for differential apparent fractionation by plant functional type.

Several approaches have been developed to estimate ϵ_p through time in response to changes in vegetation composition. Sub-fossil pollen in geologic archives has been used to infer the vegetation composition and estimate ϵ_p. Pollen abundance inform the proportion of C_3 grasses, C_4 grasses, and trees on the landscape, from which ϵ_p can be reconstructed with a four end member isotope mixing model (Feakins, 2013; Inglis et al., 2020). Fossil pollen offers high taxonomic resolution, but only for aerially dispersed pollen. In the tropics, pollen dispersed by insects and mammals are common and would be heavily underrepresented in fossil pollen records. An alternative approach uses paired measurements of $\delta^{13}C_{wax}$ to identify the vegetation community that formed the measured leaf wax because C_3, which tend to be eudicots, and C_4 plants, which tend to be grasses, have distinct $\delta^{13}C$ values (Tierney et al., 2017).

A Bayesian mixing model deconvolves the input of leaf waxes from C_3 and C_4 plants in a geologic through time, and allows us to apply the appropriate ϵ_p. Since this approach is Bayesian, uncertainties from $\delta^{13}C_{wax}$ are propogated through the record, and the full range of possible ϵ_p values is considered. This approach also has the benefit of estimating ϵ_p from the same leaf wax biomarkers that are used to measure δD_{wax}. This is the approach we use here and reconstructed ϵ_p is strikingly similar to contemporary surveys in the Amazon. The median ϵ_p for all samples at ODP1239 is close to -125‰ (Figure S2) and contemporary observations demonstrate an ϵ_p of -125‰(Feakins et al., 2016).

Station	Latitude (°)	Longitude (°)	Sampling Period	Niño 1+2 Anomaly (°C)	Niño 3.4 Anomaly (°C)	Reference
Alluriquin	-0.317	-78.97	July 1992 - June 1993	0.17	0.27	(Garcia et al., 1998)
Amaluza	-2.6	-78.57	May 1992 - April 1993	0.21	0.20	(Garcia et al., 1998)
Esmeraldas	0.97	-79.63	July 1992 - June 1993	0.17	0.27	(Garcia et al., 1998)
La Concordia	0.1047	-79.23	July 1992 - June 1993	0.17	0.27	(Garcia et al., 1998)
Uzhcurrumi	-3.32	-79.6	May 1992 - April 1994	0.09	0.61	(Garcia et al., 1998)

Table S1: GNIP Stations used within this study. Note, all stations experienced neutral El Niño conditions during the sampling interval. The Niño 1+2 and 3.4 Anomaly is calculated relative to the 1981-2010 mean. Station names are colored according to Figure 1E.

	Model	Conditional R^2	Marginal R^2	Log-Likelihood	1AIC
1	Monthly precipitation weighted $\delta D_p \sim 1$ + random(Elevation)	0.04	0	-267.31	1558.62
2	Monthly precipitation weighted $\delta D_p \sim$ West Ecuador Zonal Wind** + Monthly Precipitation + random(Elevation)*	0.57	0.49	-254.25	1518.51
3	Monthly precipitation weighted $\delta D_p \sim$ West Ecuador Zonal Wind** + random(Elevation)*	0.56	0.48	-254.90	1517.79
4	Monthly precipitation weighted $\delta D_p \sim$ Monthly Precipitation** + random(Elevation)	0.33	0.25	-268.11	1544.23
5	$\sqrt[3]{\text{Monthly precipitation weighted } \delta D_p} \sim 1$ + random(Elevation)	0.04	0	-109.14	1224.28
6	$\sqrt[3]{\text{Monthly precipitation weighted } \delta D_p} \sim$ West Ecuador Zonal Wind** + Monthly Precipitation + random(Elevation)	0.43	0.37	-94.68	1199.37
7	$\sqrt[3]{\text{Monthly precipitation weighted } \delta D_p} \sim$ West Ecuador Zonal Wind** + random(Elevation)	0.41	0.35	-95.58	1199.16
8	$\sqrt[3]{\text{Monthly precipitation weighted } \delta D_p} \sim$ Monthly Precipitation** + random(Elevation)	0.28	0.21	-102.20	1212.41

Table S2: The linear mixed-effects models tested to determine the climatological controls on monthly precipitation weighted δD_p from GNIP and the resulting conditional R^2, marginal R^2, log-likelihood, and Akaike information criterion as model diagnostics (Akaike, 1973; Nakagawa and Schielzeth, 2013). The random(Elevation) term corresponds to the random effect of station elevation, thereby allowing different intercepts for the fixed effect in the linear mixed-effects model (i.e. the same slope but with different intercepts). This term was included in all models tested because the relationship between Monthly Weighted δD_p varies strongly by elevation. Statistical significance of linear mixed effect model terms (p-value) is indicated with *, where * indicates $0.05 < p < 0.1$ and ** indicates $p \leq 0.05$.

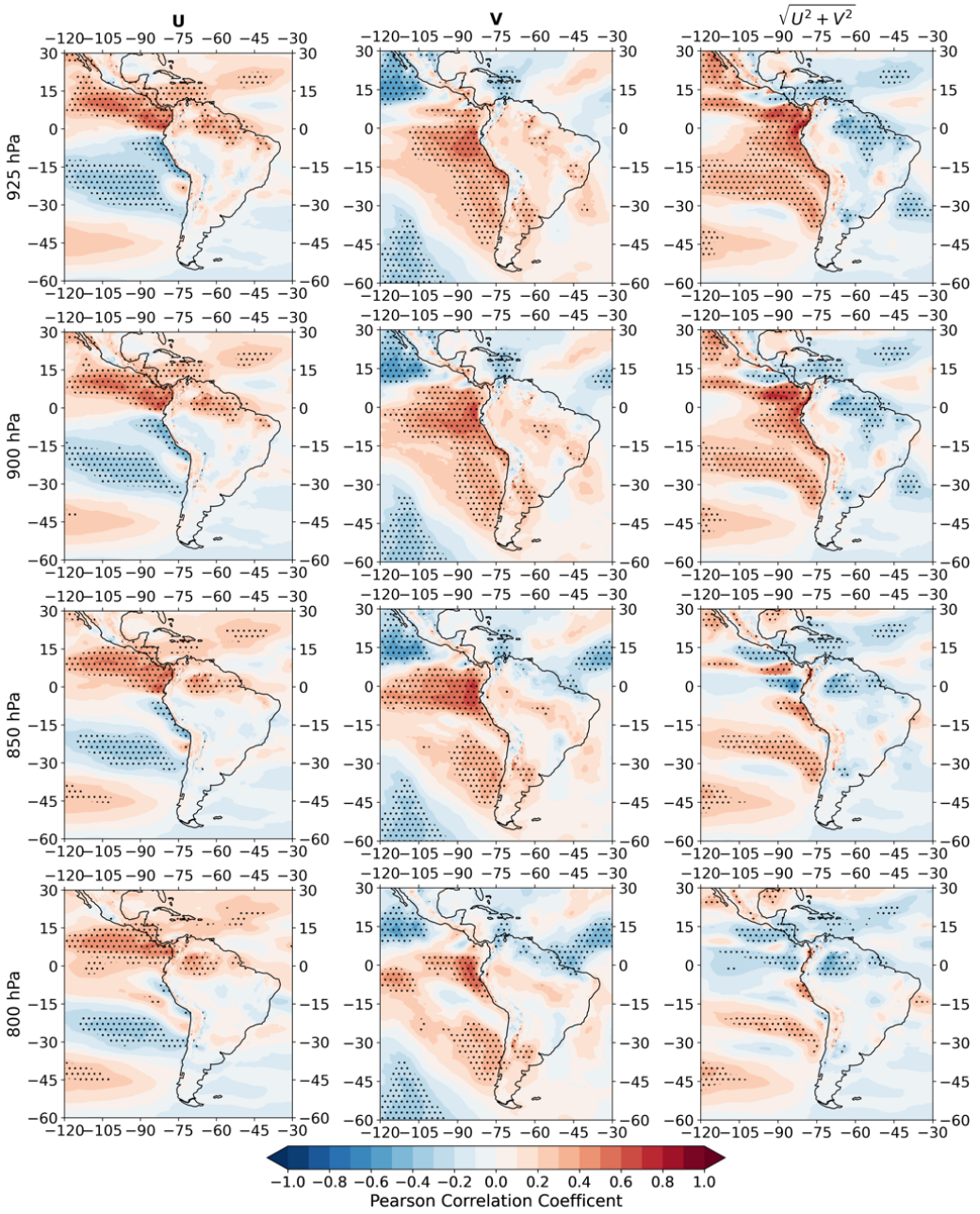

Figure S1: The correlation between west Ecuador zonal winds and zonal, meridional, and wind magnitude at the 925, 900, 850, and 800 hPa pressure levels calculated based on data from ERA5 for annual averages between 1959 and 2022 (Hersbach et al., 2020). Each column corresponds to a correlation between west Ecuador zonal winds and a different component of wind. Each row corresponds to a different pressure level. Stippling indicates significance at the 95% confidence level based on a Student's t-test. At all pressure levels, west Ecuador zonal winds are correlated with westerly transport from the Eastern Pacific Warm Pool, where δD_{vapor} is enriched in deuterium (Figure S6), toward western Ecuador.

Figure S2: Each panel correspond to the probability density function of modeled ϵ_p for every δD_{wax} sample at ODP1239 from the Bayesian isotope mixing model employed to reconstruct δD_p. Each panel title corresponds to the depth (mcd) of the sample.

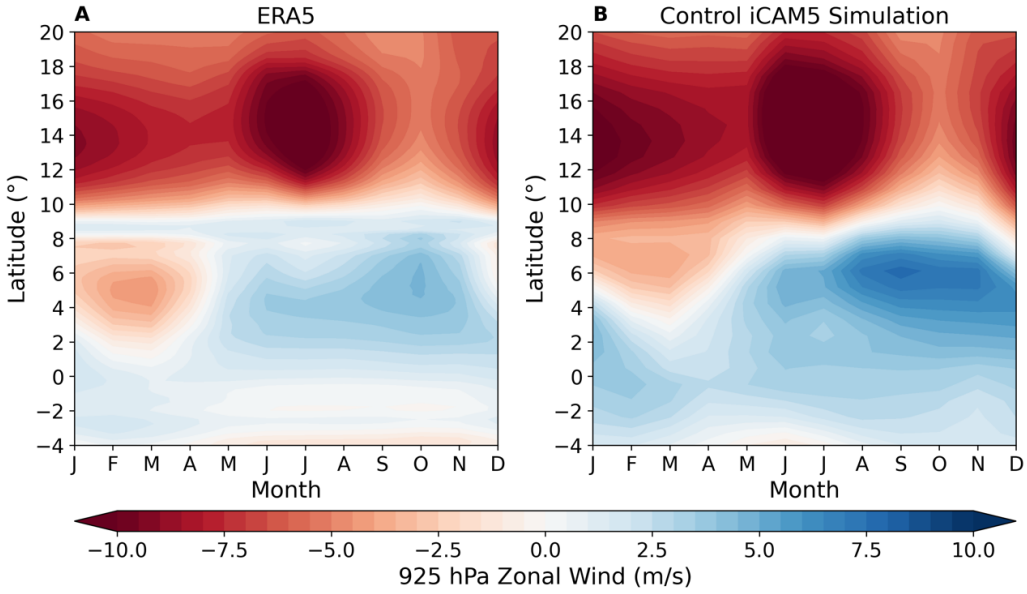

Figure S3: Hövmoller diagrams of 925 hPa zonal winds at 81 °W from (A) ERA5 (Hersbach et al., 2020) and (B) the control iCAM5 simulation (Knapp et al., 2022b). The control iCAM5 simulation captures the meridional migration of the Choco jet and strengthening in SON. The climatology for ERA5 is based on the period 1959 to 2022.

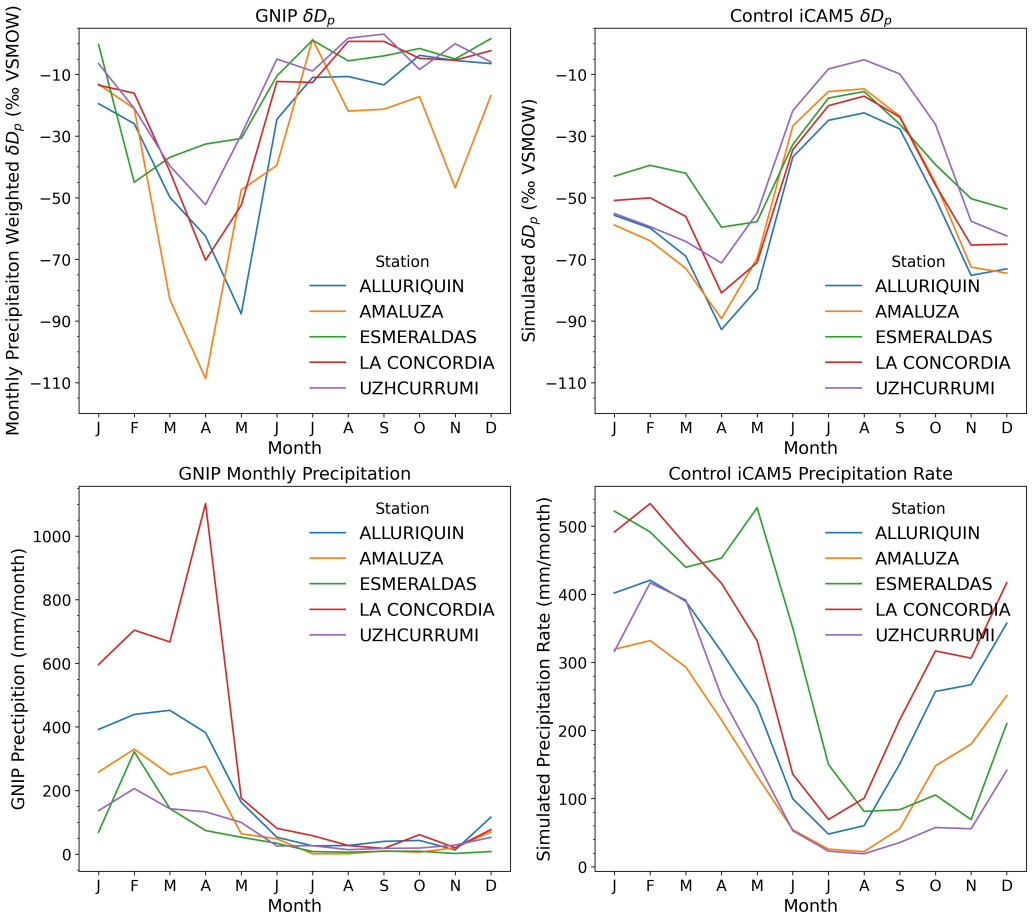

Figure S4: (Top Left) Monthly precipitation weighted δD$_p$ from the five GNIP stations analyzed (as in Figure 1D). (Top Right) Monthly δD$_p$ from the control iCAM5 simulation for the grid cell nearest to the five GNIP stations analyzed. (Bottom Right) Monthly precipitation from the GNIP stations. (Bottom Left) Monthly precipitaiton rate from iCAM5.

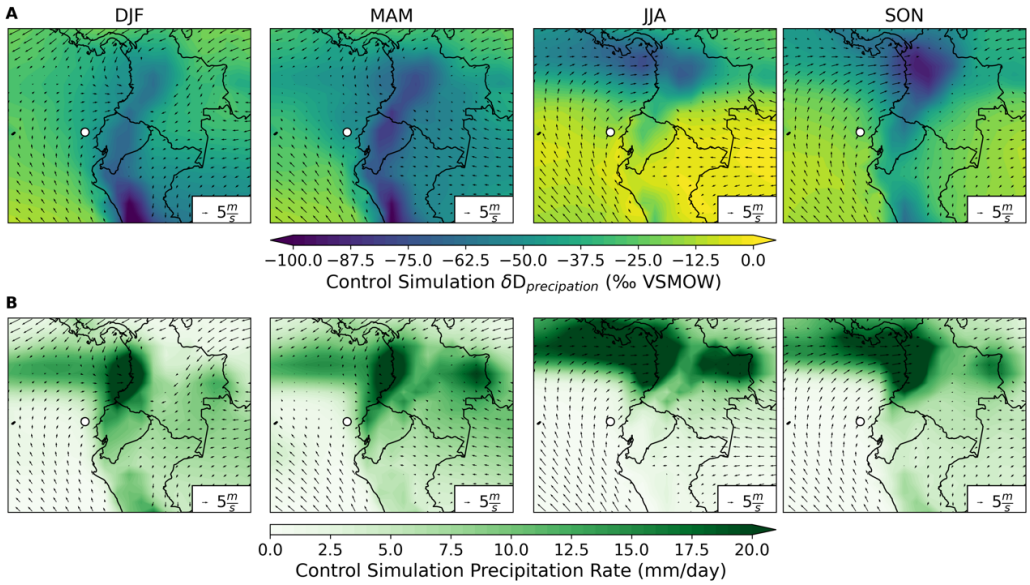

Figure S5: Seasonal climatology of (A) δD_p and (B) precipitation from the control iCAM5 simulation (Knapp et al., 2022b). More negative δD_p from GNIP stations in western Ecuador is captured, as is the unimodal precipitation regime (Figure 1). The location of ODP1239 is labeled as a white point.

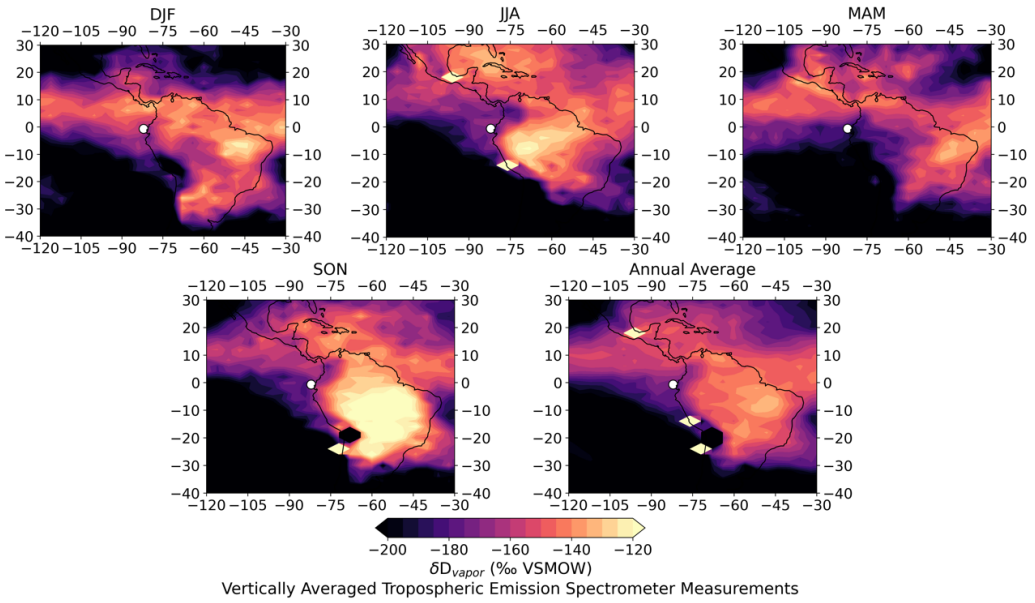

Figure S6: The seasonal and annual climatology of pressure-weighted δD_{vapor} averaged between 825 and 450 hPa based on the Version 4 Level 3 Tropospheric Emission Spectrometer satellite data product for the years 2006, 2007, 2008, and 2009. Note the δD_{vapor} enriched in deuterium from the eastern Pacific ITCZ extending to northwestern South America for all seasons except MAM.

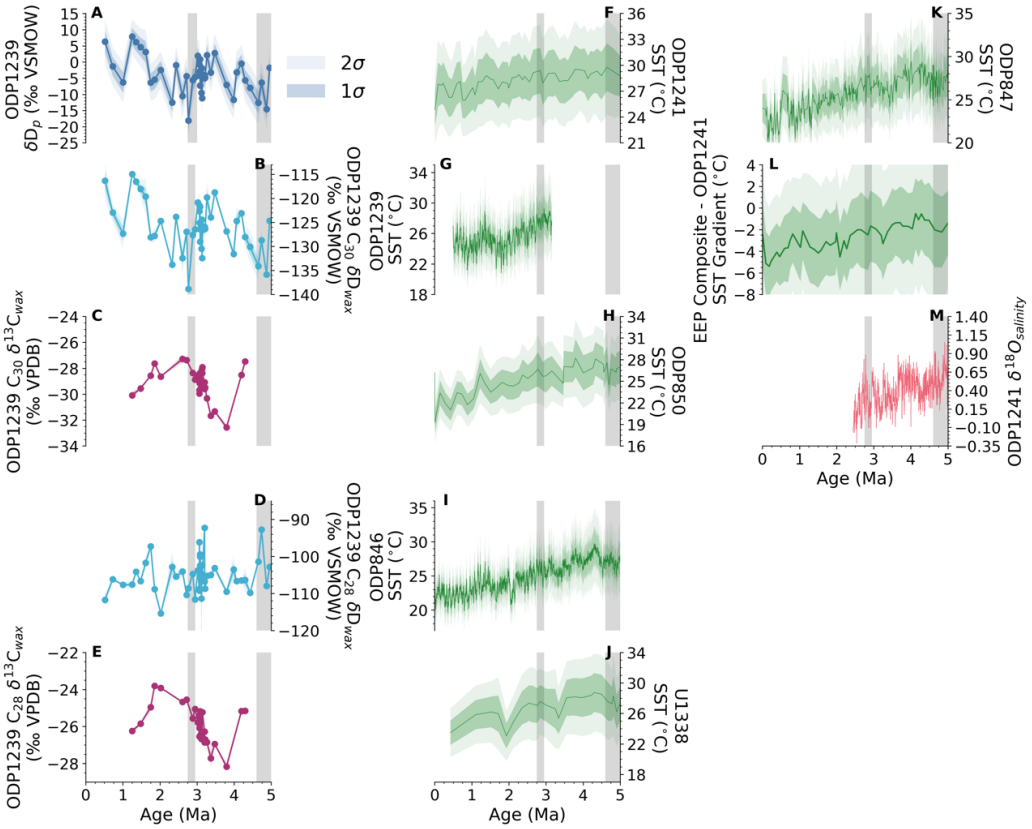

Figure S7: (A) Reconstructed δD_p at ODP1239 as shown in Figure 3A based on C_{30} *n*-alkanoic acids. (B) δD_{wax} and (C) $\delta^{13}C_{wax}$ of C_{30} *n*-alkanoic acids at ODP1239. (D) δD_{wax} and (E) $\delta^{13}C_{wax}$ of C_{28} *n*-alkanoic acids at ODP1239. (F-K) Reconstructed alkenone SSTs from ODP1241 (Seki et al., 2012), ODP1239 (Etourneau et al., 2010), ODP850 (Zhang et al., 2014b), ODP846 (Lawrence et al., 2006), IODP U1338 (Rousselle et al., 2013), and ODP847 (Dekens et al., 2007) calibrated using BAYSPLINE (Tierney and Tingley, 2018). (L) The SST gradient between the cold tongue and off-equatorial (ODP1241) region of the eastern equatorial Pacific, as in Figure 3B. (M) $\delta^{18}O_{salinity}$ at ODP1239 as in Figure 3C. The shaded area corresponds to the early Pliocene (5.0 to 4.6 Ma) and the onset of major Northern Hemisphere glaciation (3.0 to 2.75 Ma).

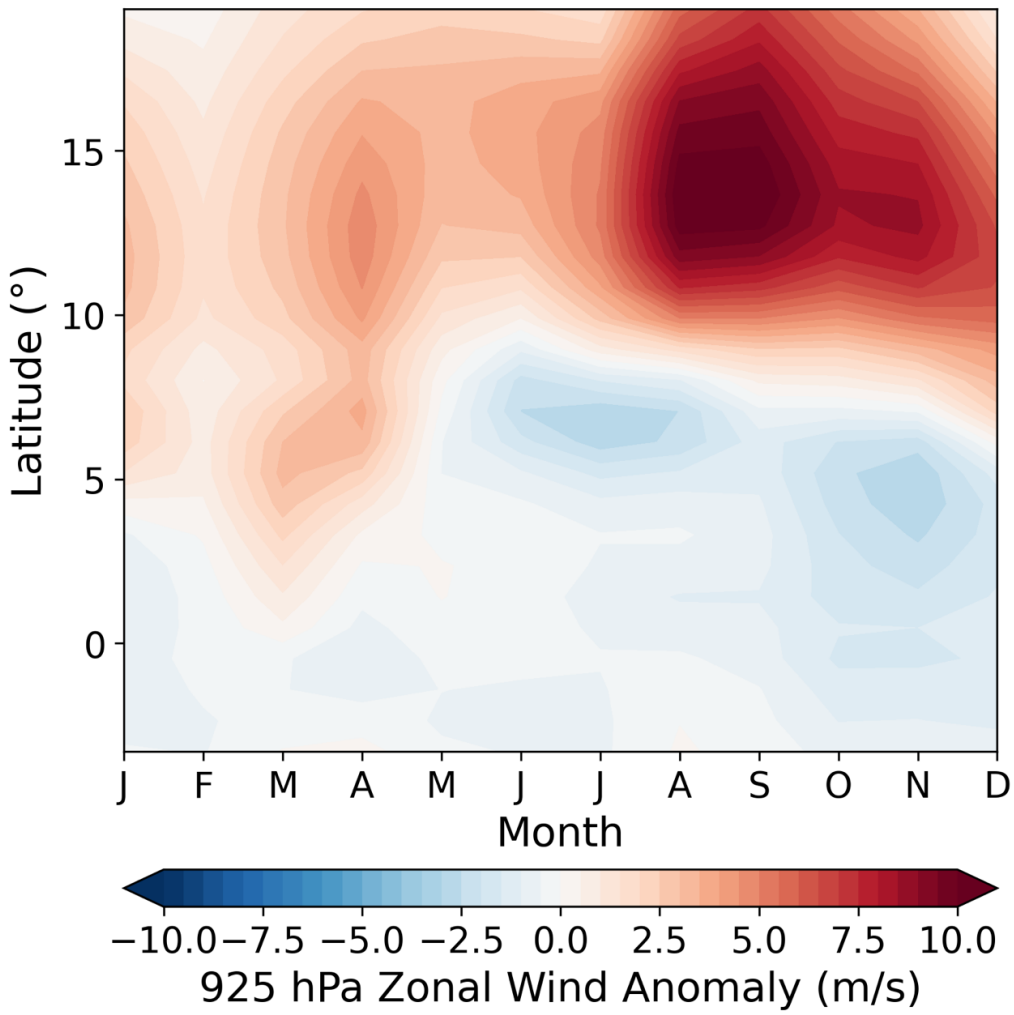

Figure S8: Hövmoller diagram of 925 hPa zonal wind anomalies (early Pliocene experiment - control) at 81 °W.

References

Aggarwal, P.K., Alduchov, O., Araguás Araguás, L., Dogramaci, S., Katzlberger, G., Kriz, K., Kulkarni, K.M., Kurttas, T., Newman, B.D., Purcher, A., 2007. New capabilities for studies using isotopes in the water cycle. Eos, Transactions American Geophysical Union 88, 537–538. doi:10.1029/2007EO490002.

Akaike, H., 1973. Information Theory and an Extension of the Maximum Likelihood Principle, in: Petrov, B.N., Csaki, F. (Eds.), Proceedings of the 2nd International Symposium on Information Theory. Akademiai Kiado, Budapest, pp. 267–281.

Ambach, W., Dansgaard, W., Eisner, H., Møller, J., 1968. The altitude effect on the isotopic composition of precipitation and glacier ice in the Alps. Tellus 20, 595–600. doi:10.1111/j.2153-3490.1968.tb00402.x.

Amundson, R., Dietrich, W., Bellugi, D., Ewing, S., Nishiizumi, K., Chong, G., Owen, J., Finkel, R., Heimsath, A., Stewart, B., Caffee, M., 2012. Geomorphologic evidence for the late Pliocene onset of hyperaridity in the Atacama Desert. GSA Bulletin 124, 1048–1070. doi:10.1130/B30445.1.

Barrett, B.S., Hameed, S., 2017. Seasonal Variability in Precipitation in Central and Southern Chile: Modulation by the South Pacific High. Journal of Climate 30, 55–69. doi:10.1175/JCLI-D-16-0019.1.

Bhattacharya, T., Feng, R., Tierney, J.E., Rubbelke, C., Burls, N., Knapp, S., Fu, M., 2022. Expansion and Intensification of the North American Monsoon During the Pliocene. AGU Advances 3, e2022AV000757. doi:10.1029/2022AV000757.

Bhattacharya, T., Tierney, J.E., Addison, J.A., Murray, J.W., 2018. Ice-sheet modulation of deglacial North American monsoon intensification. Nature Geoscience 11, 848–+. doi:10.1038/s41561-018-0220-7.

Bjerknes, J., 1969. Atmospheric teleconnections from the equatorial Pacific. Monthly Weather Review 97, 163–172. doi:10.1175/1520-0493(1969)097<0163:ATFTEP>2.3.CO;2.

Brady, E., Stevenson, S., Bailey, D., Liu, Z., Noone, D., Nusbaumer, J., Otto-Bliesner, B.L., Tabor, C., Tomas, R., Wong, T., Zhang, J., Zhu,

J., 2019. The Connected Isotopic Water Cycle in the Community Earth System Model Version 1. Journal of Advances in Modeling Earth Systems 11, 2547–2566. doi:10.1029/2019MS001663.

Broccoli, A.J., Dahl, K.A., Stouffer, R.J., 2006. Response of the ITCZ to Northern Hemisphere cooling. Geophysical Research Letters 33. doi:10.1029/2005gl024546.

Burls, N.J., Fedorov, A.V., 2014. Simulating Pliocene warmth and a permanent El Niño-like state: The role of cloud albedo. Paleoceanography 29, 893–910. doi:10.1002/2014PA002644.

Chiang, J.C.H., Biasutti, M., Battisti, D.S., 2003. Sensitivity of the Atlantic Intertropical Convergence Zone to Last Glacial Maximum boundary conditions. Paleoceanography 18. doi:Artn 1094 10.1029/2003pa000916.

Chiang, J.C.H., Bitz, C.M., 2005. Influence of high latitude ice cover on the marine Intertropical Convergence Zone. Climate Dynamics 25, 477–496. doi:10.1007/s00382-005-0040-5.

Dansgaard, W., 1964. Stable isotopes in precipitation. Tellus 16, 436–468.

Dee, S., Bailey, A., Conroy, J.L., Atwood, A., Stevenson, S., Nusbaumer, J., Noone, D., 2023. Water isotopes, climate variability, and the hydrological cycle: Recent advances and new frontiers. Environmental Research: Climate 2, 022002. doi:10.1088/2752-5295/accbe1.

Dekens, P.S., Ravelo, A.C., McCarthy, M.D., 2007. Warm upwelling regions in the Pliocene warm period. Paleoceanography 22. doi:10.1029/2006PA001394.

Echeverri, S., Cardona, A., Pardo, A., Monsalve, G., Valencia, V.A., Borrero, C., Rosero, S., López, S., 2015. Regional provenance from southwestern Colombia fore-arc and intra-arc basins: Implications for Middle to Late Miocene orogeny in the Northern Andes. Terra Nova 27, 356–363. doi:10.1111/ter.12167.

Eglinton, G., Hamilton, R.J., 1967. Leaf epicuticular waxes. Science 156, 1322–+. doi:10.1126/science.156.3780.1322.

Ehleringer, J.R., Dawson, T.E., 1992. Water uptake by plants: Perspectives from stable isotope composition. Plant, Cell & Environment 15, 1073–1082. doi:10.1111/j.1365-3040.1992.tb01657.x.

Emck, P., 2007. A Climatology of South Ecuador-with Special Focus on the Major Andean Ridge as Atlantic-Pacific Climate Divide. Ph.D. thesis. Friedrich-Alexander-Universität Erlangen-Nürnberg (FAU).

Etourneau, J., Schneider, R., Blanz, T., Martinez, P., 2010. Intensification of the Walker and Hadley atmospheric circulations during the Pliocene–Pleistocene climate transition. Earth and Planetary Science Letters 297, 103–110. doi:10.1016/j.epsl.2010.06.010.

Fahad, A.A., Burls, N.J., Swenson, E.T., Straus, D.M., 2021. The Influence of South Pacific Convergence Zone Heating on the South Pacific Subtropical Anticyclone. Journal of Climate 34, 3787–3798. doi:10.1175/JCLI-D-20-0509.1.

Fastovich, D., Bhattacharya, T., Pérez-Ángel, L., Burls, N., Feng, R., Knapp, S., Mayer, T., 2023. Plio-Pleistocene evolution of westerly moisture transport into the northern tropical Andes. Zenodo. doi:10.5281/ZENODO.10301984.

Feakins, S.J., 2013. Pollen-corrected leaf wax D/H reconstructions of northeast African hydrological changes during the late Miocene. Palaeogeography, Palaeoclimatology, Palaeoecology 374, 62–71. doi:10.1016/j.palaeo.2013.01.004.

Feakins, S.J., Bentley, L.P., Salinas, N., Shenkin, A., Blonder, B., Goldsmith, G.R., Ponton, C., Arvin, L.J., Wu, M.S., Peters, T., West, A.J., Martin, R.E., Enquist, B.J., Asner, G.P., Malhi, Y., 2016. Plant leaf wax biomarkers capture gradients in hydrogen isotopes of precipitation from the Andes and Amazon. Geochimica et Cosmochimica Acta 182, 155–172. doi:10.1016/j.gca.2016.03.018.

Feakins, S.J., Sessions, A.L., 2010. Controls on the D/H ratios of plant leaf waxes in an arid ecosystem. Geochimica et Cosmochimica Acta 74, 2128–2141. doi:10.1016/j.gca.2010.01.016.

Fedorov, A.V., Burls, N.J., Lawrence, K.T., Peterson, L.C., 2015. Tightly linked zonal and meridional sea surface temperature gradients over the past five million years. Nature Geoscience 8, 975–980. doi:10.1038/ngeo2577.

Fedorov, A.V., Dekens, P.S., McCarthy, M., Ravelo, A.C., deMenocal, P.B., Barreiro, M., Pacanowski, R.C., Philander, S.G., 2006. The Pliocene Paradox (Mechanisms for a Permanent El Niño). Science 312, 1485–1489. doi:10.1126/science.1122666.

Ford, H.L., Ravelo, A.C., Dekens, P.S., LaRiviere, J.P., Wara, M.W., 2015. The evolution of the equatorial thermocline and the early Pliocene El Padre mean state. Geophysical Research Letters 42, 4878–4887. doi:10.1002/2015GL064215.

Gao, L., Edwards, E.J., Zeng, Y., Huang, Y., 2014. Major Evolutionary Trends in Hydrogen Isotope Fractionation of Vascular Plant Leaf Waxes. PLOS ONE 9, e112610. doi:10.1371/journal.pone.0112610.

Garcia, M., Villalba, F., Araguas-Araguas, L., Rozanski, K., 1998. The role of atmospheric circulation patterns in controlling the regional distribution of stable isotope contents in precipitation: Preliminary results from two transects in the Ecuadorian Andes, in: Isotope Techniques in the Study of Environmental Change. International Atomic Energy Agency, Vienna, Austria, pp. 127–140.

Garcia-Delgado, H., Petley, D.N., Bermúdez, M.A., Sepúlveda, S.A., 2022. Fatal landslides in Colombia (from historical times to 2020) and their socioeconomic impacts. Landslides 19, 1689–1716. doi:10.1007/s10346-022-01870-2.

Gébelin, A., Witt, C., Radkiewicz, M., Mulch, A., 2021. Impact of the Southern Ecuadorian Andes on Oxygen and Hydrogen Isotopes in Precipitation. Frontiers in Earth Science 9. doi:10.3389/feart.2021.664590.

Grimmer, F., Dupont, L., Lamy, F., Jung, G., González, C., Wefer, G., 2018. Early Pliocene vegetation and hydrology changes in western equatorial South America. Climate of the Past 14, 1739–1754. doi:10.5194/cp-14-1739-2018.

Grimmer, F., Dupont, L.M., Jung, G., Wefer, G., 2020. Piacenzian Environmental Change and the Onset of Cool and Dry Conditions in

Tropical South America. Paleoceanography and Paleoclimatology 35, e2020PA004060. doi:10.1029/2020PA004060.

Groeneveld, J., 2005. Effect of the Pliocene Closure of the Panamanian Gateway on Caribbean and East Pacific Sea Surface Temperatures and Salinities by Applying Combined Mg/Ca and d18O Measurements (5.6 - 2.2 Ma). Ph.D. thesis.

Groeneveld, J., Hathorne, E.C., Steinke, S., DeBey, H., Mackensen, A., Tiedemann, R., 2014. Glacial induced closure of the Panamanian Gateway during Marine Isotope Stages (MIS) 95–100 (∼2.5 Ma). Earth and Planetary Science Letters 404, 296–306. doi:10.1016/j.epsl.2014.08.007.

Hartley, A.J., Chong, G., 2002. Late Pliocene age for the Atacama Desert: Implications for the desertification of western South America. Geology 30, 43–46. doi:10.1130/0091-7613(2002)030<0043:LPAFTA>2.0.CO;2.

Herbert, T.D., Lawrence, K.T., Tzanova, A., Peterson, L.C., Caballero-Gill, R., Kelly, C.S., 2016. Late Miocene global cooling and the rise of modern ecosystems. Nature Geoscience 9, 843–847. doi:10.1038/ngeo2813.

Hersbach, H., Bell, B., Berrisford, P., Hirahara, S., Horányi, A., Muñoz-Sabater, J., Nicolas, J., Peubey, C., Radu, R., Schepers, D., Simmons, A., Soci, C., Abdalla, S., Abellan, X., Balsamo, G., Bechtold, P., Biavati, G., Bidlot, J., Bonavita, M., De Chiara, G., Dahlgren, P., Dee, D., Diamantakis, M., Dragani, R., Flemming, J., Forbes, R., Fuentes, M., Geer, A., Haimberger, L., Healy, S., Hogan, R.J., Hólm, E., Janisková, M., Keeley, S., Laloyaux, P., Lopez, P., Lupu, C., Radnoti, G., de Rosnay, P., Rozum, I., Vamborg, F., Villaume, S., Thépaut, J.N., 2020. The ERA5 global reanalysis. Quarterly Journal of the Royal Meteorological Society 146, 1999–2049. doi:10.1002/qj.3803.

Heusser, L.E., Shackleton, N.J., 1994. Tropical Climatic Variation on the Pacific Slopes of the Ecuadorian Andes Based on a 25,000-Year Pollen Record from Deep-Sea Sediment Core Tri 163-31B. Quaternary Research 42, 222–225. doi:10.1006/qres.1994.1072.

Hou, J., D'Andrea, W.J., Huang, Y., 2008. Can sedimentary leaf waxes record D/H ratios of continental precipitation? Field, model, and experimental assessments. Geochimica et Cosmochimica Acta 72, 3503–3517. doi:10.1016/j.gca.2008.04.030.

Hovan, S.A., 1995. 28. Late Cenozoic atmospheric circulation intensity and climatic history recorded by Eolian deposition in the Eastern Equatorial Pacific Ocean, Leg 138. Proceedings of the Ocean Drilling Program, Scientific Results. Proceedings of the Ocean Drilling Program, Scientific Results , 615–625.

Hoyos, I., Cañón-Barriga, J., Arenas-Suárez, T., Dominguez, F., Rodríguez, B.A., 2019. Variability of regional atmospheric moisture over Northern South America: Patterns and underlying phenomena. Climate Dynamics 52, 893–911. doi:10.1007/s00382-018-4172-9.

Hoyos, I., Dominguez, F., Cañón-Barriga, J., Martínez, J.A., Nieto, R., Gimeno, L., Dirmeyer, P.A., 2018. Moisture origin and transport processes in Colombia, northern South America. Climate Dynamics 50, 971–990. doi:10.1007/s00382-017-3653-6.

Hu, J., Emile-Geay, J., Nusbaumer, J., Noone, D., 2018. Impact of Convective Activity on Precipitation δ18O in Isotope-Enabled General Circulation Models. Journal of Geophysical Research: Atmospheres 123, 13,595–13,610. doi:10.1029/2018JD029187.

Inglis, G.N., Bhattacharya, T., Hemingway, J.D., Hollingsworth, E.H., Feakins, S.J., Tierney, J.E., 2022. Biomarker Approaches for Reconstructing Terrestrial Environmental Change. Annual Review of Earth and Planetary Sciences 50, 369–394. doi:10.1146/annurev-earth-032320-095943.

Inglis, G.N., Carmichael, M.J., Farnsworth, A., Lunt, D.J., Pancost, R.D., 2020. A long-term, high-latitude record of Eocene hydrological change in the Greenland region. Palaeogeography, Palaeoclimatology, Palaeoecology 537, 109378. doi:10.1016/j.palaeo.2019.109378.

Ishii, M., Shouji, A., Sugimoto, S., Matsumoto, T., 2005. Objective analyses of sea-surface temperature and marine meteorological variables for the 20th century using ICOADS and the Kobe Collection. International Journal of Climatology 25, 865–879. doi:10.1002/joc.1169.

Knapp, S., Burls, N., Dee, S., Feng, R., Feakins, S.J., Bhattacharya, T., 2022a. Data for article "A Pliocene precipitation isotope proxy-model comparison assessing the hydrological fingerprints of sea surface temperature gradients" doi:10.5281/ZENODO.6953979.

Knapp, S., Burls, N.J., Dee, S., Feng, R., Feakins, S.J., Bhattacharya, T., 2022b. A Pliocene Precipitation Isotope Proxy-Model Comparison Assessing the Hydrological Fingerprints of Sea Surface Temperature Gradients. Paleoceanography and Paleoclimatology 37, e2021PA004401. doi:10.1029/2021PA004401.

Kusch, S., Rethemeyer, J., Schefuß, E., Mollenhauer, G., 2010. Controls on the age of vascular plant biomarkers in Black Sea sediments. Geochimica et Cosmochimica Acta 74, 7031–7047. doi:10.1016/j.gca.2010.09.005.

Lawrence, K.T., Liu, Z., Herbert, T.D., 2006. Evolution of the Eastern Tropical Pacific Through Plio-Pleistocene Glaciation. Science 312, 79–83. doi:10.1126/science.1120395.

León, S., Cardona, A., Parra, M., Sobel, E.R., Jaramillo, J.S., Glodny, J., Valencia, V.A., Chew, D., Montes, C., Posada, G., Monsalve, G., Pardo-Trujillo, A., 2018. Transition From Collisional to Subduction-Related Regimes: An Example From Neogene Panama-Nazca-South America Interactions. Tectonics 37, 119–139. doi:10.1002/2017TC004785.

Lindzen, R.S., Nigam, S., 1987. On the Role of Sea Surface Temperature Gradients in Forcing Low-Level Winds and Convergence in the Tropics. Journal of the Atmospheric Sciences 44, 2418–2436. doi:10.1175/1520-0469(1987)044<2418:OTROSS>2.0.CO;2.

Lisiecki, L.E., Raymo, M.E., 2005. A Pliocene-Pleistocene stack of 57 globally distributed benthic delta O-18 records. Paleoceanography 20, PA1003. doi:10.1029/2004pa001071.

Liu, J., An, Z., 2020. Leaf wax n-alkane carbon isotope values vary among major terrestrial plant groups: Different responses to precipitation amount and temperature, and implications for paleoenvironmental reconstruction. Earth-Science Reviews 202, 103081. doi:10.1016/j.earscirev.2020.103081.

Liu, J., Tian, J., Liu, Z., Herbert, T.D., Fedorov, A.V., Lyle, M., 2019. Eastern equatorial Pacific cold tongue evolution since the late Miocene linked to extratropical climate. Science Advances 5, eaau6060. doi:10.1126/sciadv.aau6060.

Locarnini, R.A., Mishonov, A.V., Antonov, J.I., Boyer, T.P., Garcia, H.E., Baranova, O.K., Zweng, M.M., Paver, C.R., Reagan, J.R., Johnson, D.R.,

Hamilton, M., Seidov, 1948, D., Levitus, S., 2013. World ocean atlas 2013. Volume 1, Temperature doi:10.7289/V55X26VD.

Marchant, R., Almeida, L., Behling, H., Berrio, J.C., Bush, M., Cleef, A., Duivenvoorden, J., Kappelle, M., De Oliveira, P., Teixeira de Oliveira-Filho, A., Lozano-Garćia, S., Hooghiemstra, H., Ledru, M.P., Ludlow-Wiechers, B., Markgraf, V., Mancini, V., Paez, M., Prieto, A., Rangel, O., Salgado-Labouriau, M.L., 2002. Distribution and ecology of parent taxa of pollen lodged within the Latin American Pollen Database. Review of Palaeobotany and Palynology 121, 1–75. doi:10.1016/S0034-6667(02)00082-9.

Margirier, A., Strecker, M.R., Reiners, P.W., Thomson, S.N., Casado, I., George, S.W.M., Alvarado, A., 2023. Late Miocene Exhumation of the Western Cordillera, Ecuador, Driven by Increased Coupling Between the Subducting Carnegie Ridge and the South American Continent. Tectonics 42, e2022TC007344. doi:10.1029/2022TC007344.

Martínez, I., Keigwin, L., Barrows, T.T., Yokoyama, Y., Southon, J., 2003. La Niña-like conditions in the eastern equatorial Pacific and a stronger Choco jet in the northern Andes during the last glaciation. Paleoceanography 18. doi:10.1029/2002PA000877.

Martínez-Botí, M.A., Foster, G.L., Chalk, T.B., Rohling, E.J., Sexton, P.F., Lunt, D.J., Pancost, R.D., Badger, M.P.S., Schmidt, D.N., 2015. Plio-Pleistocene climate sensitivity evaluated using high-resolution CO2 records. Nature 518, 49–54. doi:10.1038/nature14145.

Meinicke, N., Reimi, M.A., Ravelo, A.C., Meckler, A.N., 2021. Coupled Mg/Ca and Clumped Isotope Measurements Indicate Lack of Substantial Mixed Layer Cooling in the Western Pacific Warm Pool During the Last ∼5 Million Years. Paleoceanography and Paleoclimatology 36, e2020PA004115. doi:10.1029/2020PA004115.

Mix, A., Tiedemann, R., Blum, P., et al. (Eds.), 2003. Proceedings of the Ocean Drilling Program, 202 Initial Reports. volume 202 of *Proceedings of the Ocean Drilling Program*. Ocean Drilling Program. doi:10.2973/odp.proc.ir.202.2003.

Morán-Tejeda, E., Bazo, J., López-Moreno, J.I., Aguilar, E., Azorín-Molina, C., Sanchez-Lorenzo, A., Martínez, R., Nieto, J.J., Mejía, R., Martín-Hernández, N., Vicente-Serrano, S.M., 2016. Climate trends and variability in Ecuador (1966–2011). International Journal of Climatology 36, 3839–3855. doi:10.1002/joc.4597.

Myers, N., Mittermeier, R.A., Mittermeier, C.G., da Fonseca, G.A.B., Kent, J., 2000. Biodiversity hotspots for conservation priorities. Nature 403, 853–858. doi:10.1038/35002501.

Nakagawa, S., Schielzeth, H., 2013. A general and simple method for obtaining R2 from generalized linear mixed-effects models. Methods in Ecology and Evolution 4, 133–142. doi:10.1111/j.2041-210x.2012.00261.x.

O'Dea, A., Lessios, H.A., Coates, A.G., Eytan, R.I., Restrepo-Moreno, S.A., Cione, A.L., Collins, L.S., de Queiroz, A., Farris, D.W., Norris, R.D., Stallard, R.F., Woodburne, M.O., Aguilera, O., Aubry, M.P., Berggren, W.A., Budd, A.F., Cozzuol, M.A., Coppard, S.E., Duque-Caro, H., Finnegan, S., Gasparini, G.M., Grossman, E.L., Johnson, K.G., Keigwin, L.D., Knowlton, N., Leigh, E.G., Leonard-Pingel, J.S., Marko, P.B., Pyenson, N.D., Rachello-Dolmen, P.G., Soibelzon, E., Soibelzon, L., Todd, J.A., Vermeij, G.J., Jackson, J.B.C., 2016. Formation of the Isthmus of Panama. Science Advances 2, e1600883. doi:10.1126/sciadv.1600883.

Osorio-Granada, E., Restrepo-Moreno, S.A., Muñoz-Valencia, J.A., Trejos-Tamayo, R.A., Pardo-Trujillo, A., Barbosa-Espitia, A.A., 2017. Detrital zircon typology and U/Pb geochronology for the Miocene Ladrilleros-Juanchaco sedimentary sequence, Equatorial Pacific (Colombia): New constraints on provenance and paleogeography in northwestern South America. Geologica Acta: an international earth science journal 15, 201–215.

Pérez-Angel, L.C., Sepúlveda, J., Montes, C., Smith, J.J., Molnar, P., González-Arango, C., Snell, K.E., Dildar, N., 2022. Mixed Signals From the Stable Isotope Composition of Precipitation and Plant Waxes in the Northern Tropical Andes. Journal of Geophysical Research: Biogeosciences 127, e2022JG006932. doi:10.1029/2022JG006932.

Polissar, P.J., Freeman, K.H., 2010. Effects of aridity and vegetation on plant-wax δD in modern lake sediments. Geochimica et Cosmochimica Acta 74, 5785–5797. doi:10.1016/j.gca.2010.06.018.

Poveda, G., Jaramillo, L., Vallejo, L.F., 2014. Seasonal precipitation patterns along pathways of South American low-level jets and aerial rivers. Water Resources Research 50, 98–118. doi:10.1002/2013WR014087.

Poveda, G., Mesa, O.J., 2000. On the existence of Lloró (the rainiest locality on Earth): Enhanced ocean-land-atmosphere interaction by a low-level jet. Geophysical Research Letters 27, 1675–1678. doi:10.1029/1999GL006091.

Poveda, G., Waylen, P.R., Pulwarty, R.S., 2006. Annual and inter-annual variability of the present climate in northern South America and southern Mesoamerica. Palaeogeography, Palaeoclimatology, Palaeoecology 234, 3–27. doi:10.1016/j.palaeo.2005.10.031.

Powell, R.L., Still, C.J., 2009. Biogeography of C3 and C4 vegetation in South America. Anais XIV Simpósio Brasileiro de Sensoriamento Remoto , 2935–2942.

Quintana, J.M., Aceituno, P., 2012. Changes in the rainfall regime along the extratropical west coast of South America (Chile): 30-43º S. Atmósfera 25, 1–22.

Ramirez-Villegas, J., Salazar, M., Jarvis, A., Navarro-Racines, C.E., 2012. A way forward on adaptation to climate change in Colombian agriculture: Perspectives towards 2050. Climatic Change 115, 611–628. doi:10.1007/s10584-012-0500-y.

Rangel, T.F., Edwards, N.R., Holden, P.B., Diniz-Filho, J.A.F., Gosling, W.D., Coelho, M.T.P., Cassemiro, F.A.S., Rahbek, C., Colwell, R.K., 2018. Modeling the ecology and evolution of biodiversity: Biogeographical cradles, museums, and graves. Science doi:10.1126/science.aar5452.

Raymo, M.E., 1994. The initiation of Northern Hemisphere glaciation. Annual Review of Earth and Planetary Sciences 22, 353–383. doi:10.1146/annurev.ea.22.050194.002033.

Rincón-Martínez, D., Lamy, F., Contreras, S., Leduc, G., Bard, E., Saukel, C., Blanz, T., Mackensen, A., Tiedemann, R., 2010. More humid interglacials in Ecuador during the past 500 kyr linked to latitudinal shifts of the equatorial front and the Intertropical Convergence Zone in the eastern tropical Pacific. Paleoceanography 25. doi:10.1029/2009PA001868.

Rossel, F., Cadier, E., 2009. El Niño and prediction of anomalous monthly rainfalls in Ecuador. Hydrological Processes 23, 3253–3260. doi:10.1002/hyp.7401.

Rousselle, G., Beltran, C., Sicre, M.A., Raffi, I., De Rafélis, M., 2013. Changes in sea-surface conditions in the Equatorial Pacific during the middle Miocene–Pliocene as inferred from coccolith geochemistry. Earth and Planetary Science Letters 361, 412–421. doi:10.1016/j.epsl.2012.11.003.

Rowley, D.B., Garzione, C.N., 2007. Stable Isotope-Based Paleoaltimetry. Annual Review of Earth and Planetary Sciences 35, 463–508. doi:10.1146/annurev.earth.35.031306.140155.

Rozanski, K., Araguás-Araguás, L., Gonfiantini, R., 1993. Isotopic Patterns in Modern Global Precipitation, in: Climate Change in Continental Isotopic Records. American Geophysical Union (AGU), pp. 1–36. doi:10.1029/GM078p0001.

Sachse, D., Billault, I., Bowen, G.J., Chikaraishi, Y., Dawson, T.E., Feakins, S.J., Freeman, K.H., Magill, C.R., McInerney, F.A., van der Meer, M.T.J., Polissar, P., Robins, R.J., Sachs, J.P., Schmidt, H.L., Sessions, A.L., White, J.W.C., West, J.B., Kahmen, A., 2012. Molecular Paleohydrology: Interpreting the Hydrogen- Isotopic Composition of Lipid Biomarkers from Photosynthesizing Organisms, in: Jeanloz, R. (Ed.), Annual Review of Earth and Planetary Sciences, Vol 40. Annual Reviews, Palo Alto. volume 40 of *Annual Review of Earth and Planetary Sciences*, pp. 221–249.

Sachse, D., Radke, J., Gleixner, G., 2004. Hydrogen isotope ratios of recent lacustrine sedimentary n-alkanes record modern climate variability. Geochimica et Cosmochimica Acta 68, 4877–4889. doi:10.1016/j.gca.2004.06.004.

Sakamoto, M.S., Ambrizzi, T., Poveda, G., 2011. Moisture Sources and Life Cycle of Convective Systems over Western Colombia. Advances in Meteorology 2011, e890759. doi:10.1155/2011/890759.

Salati, E., Dall'Olio, A., Matsui, E., Gat, J.R., 1979. Recycling of water in the Amazon Basin: An isotopic study. Water Resources Research 15, 1250–1258. doi:10.1029/WR015i005p01250.

Sauer, P.E., Eglinton, T.I., Hayes, J.M., Schimmelmann, A., Sessions, A.L., 2001. Compound-specific D/H ratios of lipid biomarkers from sediments as a proxy for environmental and climatic conditions. Geochimica et Cosmochimica Acta 65, 213–222. doi:10.1016/s0016-7037(00)00520-2.

Schneider, T., Bischoff, T., Haug, G.H., 2014. Migrations and dynamics of the intertropical convergence zone. Nature 513, 45–53. doi:10.1038/nature13636.

Schneider, U., Becker, A., Finger, P., Meyer-Christoffer, A., Rudolf, B., Ziese, M., 2011. GPCC full data reanalysis version 6.0 at 0.5: Monthly land-surface precipitation from rain-gauges built on GTS-based and historic data. GPCC Data Repository 10.

Seki, O., Schmidt, D.N., Schouten, S., Hopmans, E.C., Sinninghe Damsté, J.S., Pancost, R.D., 2012. Paleoceanographic changes in the Eastern Equatorial Pacific over the last 10 Myr. Paleoceanography 27. doi:10.1029/2011PA002158.

Sessions, A.L., Burgoyne, T.W., Schimmelmann, A., Hayes, J.M., 1999. Fractionation of hydrogen isotopes in lipid biosynthesis. Organic Geochemistry 30, 1193–1200. doi:10.1016/S0146-6380(99)00094-7.

Sierra, J.P., Arias, P.A., Durán-Quesada, A.M., Tapias, K.A., Vieira, S.C., Martínez, J.A., 2021. The Choco low-level jet: Past, present and future. Climate Dynamics 56, 2667–2692. doi:10.1007/s00382-020-05611-w.

Sierra, J.P., Arias, P.A., Vieira, S.C., 2015. Precipitation over Northern South America and Its Seasonal Variability as Simulated by the CMIP5 Models. Advances in Meteorology 2015, e634720. doi:10.1155/2015/634720.

Sierra, J.P., Arias, P.A., Vieira, S.C., Agudelo, J., 2018. How well do CMIP5 models simulate the low-level jet in western Colombia? Climate Dynamics 51, 2247–2265. doi:10.1007/s00382-017-4010-5.

Smith, F.A., Freeman, K.H., 2006. Influence of physiology and climate on δD of leaf wax n-alkanes from C3 and C4 grasses. Geochimica et Cosmochimica Acta 70, 1172–1187. doi:10.1016/j.gca.2005.11.006.

Spikings, R., Simpson, G., 2014. Rock uplift and exhumation of continental margins by the collision, accretion, and subduction of buoyant and topographically prominent oceanic crust. Tectonics 33, 635–655. doi:10.1002/2013TC003425.

Spikings, R.A., Crowhurst, P.V., Winkler, W., Villagomez, D., 2010. Syn- and post-accretionary cooling history of the Ecuadorian Andes constrained by their in-situ and detrital thermochronometric record. Journal of South American Earth Sciences 30, 121–133. doi:10.1016/j.jsames.2010.04.002.

Spikings, R.A., Winkler, W., Seward, D., Handler, R., 2001. Along-strike variations in the thermal and tectonic response of the continental Ecuadorian Andes to the collision with heterogeneous oceanic crust. Earth and Planetary Science Letters 186, 57–73. doi:10.1016/S0012-821X(01)00225-4.

Sternberg, L., 1988. D/H ratios of environmental water recorded by D/H ratios of plant lipids. Nature 333, 59–61. doi:10.1038/333059a0.

Strub, T., Mesias, J., Montecino, V., Rutllant, J., Salinas, S., 1998. Coastal ocean circulation off western South America, in: Robinson, A., Brink, K. (Eds.), The Sea, Volume 11: The Global Coastal Ocean: Regional Studies and Syntheses. Wiley, New York, pp. 273–315.

Tierney, J.E., Haywood, A.M., Feng, R., Bhattacharya, T., Otto-Bliesner, B.L., 2019. Pliocene Warmth Consistent With Greenhouse Gas Forcing. Geophysical Research Letters 46, 9136–9144. doi:10.1029/2019GL083802.

Tierney, J.E., Pausata, F.S.R., deMenocal, P.B., 2017. Rainfall regimes of the Green Sahara. Science Advances 3, e1601503. doi:10.1126/sciadv.1601503.

Tierney, J.E., Tingley, M.P., 2018. BAYSPLINE: A New Calibration for the Alkenone Paleothermometer. Paleoceanography and Paleoclimatology 33, 281–301. doi:10.1002/2017PA003201.

Timmermann, A., Lorenz, S.J., An, S.I., Clement, A., Xie, S.P., 2007. The Effect of Orbital Forcing on the Mean Climate and Variability of the Tropical Pacific. Journal of Climate 20, 4147–4159. doi:10.1175/JCLI4240.1.

Vicente-Serrano, S.M., Aguilar, E., Martínez, R., Martín-Hernández, N., Azorin-Molina, C., Sanchez-Lorenzo, A., El Kenawy, A., Tomás-Burguera,

M., Moran-Tejeda, E., López-Moreno, J.I., Revuelto, J., Beguería, S., Nieto, J.J., Drumond, A., Gimeno, L., Nieto, R., 2017. The complex influence of ENSO on droughts in Ecuador. Climate Dynamics 48, 405–427. doi:10.1007/s00382-016-3082-y.

Villagómez, D., Spikings, R., 2013. Thermochronology and tectonics of the Central and Western Cordilleras of Colombia: Early Cretaceous–Tertiary evolution of the Northern Andes. Lithos 160–161, 228–249. doi:10.1016/j.lithos.2012.12.008.

Vuille, M., Francou, B., Wagnon, P., Juen, I., Kaser, G., Mark, B.G., Bradley, R.S., 2008. Climate change and tropical Andean glaciers: Past, present and future. Earth-Science Reviews 89, 79–96. doi:10.1016/j.earscirev.2008.04.002.

Wara, M.W., Ravelo, A.C., Delaney, M.L., 2005. Permanent El Niño-Like Conditions During the Pliocene Warm Period. Science 309, 758–761. doi:10.1126/science.1112596.

Waylen, P.R., Caviedes, C.N., 1986. El Niño and annual floods on the north Peruvian littoral. Journal of Hydrology 89, 141–156. doi:10.1016/0022-1694(86)90148-4.

White, S.M., Ravelo, A.C., 2020. The Benthic B/Ca Record at Site 806: New Constraints on the Temperature of the West Pacific Warm Pool and the "El Padre" State in the Pliocene. Paleoceanography and Paleoclimatology 35, e2019PA003812. doi:10.1029/2019PA003812.

Xie, S.P., Philander, S.G.H., 1994. A coupled ocean-atmosphere model of relevance to the ITCZ in the eastern Pacific. Tellus A 46, 340–350. doi:10.1034/j.1600-0870.1994.t01-1-00001.x.

Zhang, X., Lohmann, G., Knorr, G., Purcell, C., 2014a. Abrupt glacial climate shifts controlled by ice sheet changes. Nature 512, 290.

Zhang, Y.G., Pagani, M., Liu, Z., 2014b. A 12-Million-Year Temperature History of the Tropical Pacific Ocean. Science 344, 84–87. doi:10.1126/science.1246172.